arXiv:1510.02522v1 [astro-ph.GA] 8 Oct 2015

Near-Infrared Spectroscopy of Quasars at $z \sim 3$ and Estimates of Their Supermassive Black Hole Masses

Yuriko Saito,[1,2] Masatoshi Imanishi,[1,2,3] Yosuke Minowa,[1,2] Tomoki Morokuma,[4] Toshihiro Kawaguchi,[5] Hiroaki Sameshima,[6] Takeo Minezaki,[4] Nagisa Oi,[7] Tohru Nagao,[8] Nozomu Kawatatu,[9] and Kenta Matsuoka[10]

[1]*Department of Astronomy, School of Science, Graduate University for Advanced Studies (SOKENDAI), Mitaka, Tokyo 181-8588, Japan*

yuriko.saitou@nao.ac.jp

[2]*Subaru Telescope, 650 North A'ohoku Place, Hilo, Hawaii, 96720, U.S.A.*

[3]*National Astronomical Observatory, 2-21-1, Osawa, Mitaka, Tokyo 181-8588, Japan*

[4]*Institute of Astronomy, Graduate School of Science, The University of Tokyo, 2-21-1, Osawa, Mitaka, Tokyo 181-0015, Japan*

[5]*Department of Physics, Sapporo Medical University, S1 W17, Chuo-ku, Sapporo 060-556, Japan*

[6]*Laboratory of Infrared High-resolution spectroscopy (LIH), Koyama Astronomical Observatory, Kyoto Sangyo University, Motoyama, Kamigamo, Kita-ku, Kyoto 603-8555, Japan*

[7]*Japan Aerospace Exploration Agency, Sagamihara, Kanagawa, 252-5210, Japan*

[8]*Research Center for Space and Cosmic Evolution (RCSCE), Ehime University, Bunkyo-cho 2-5, Matsuyama, Ehime 790-8577, Japan*

[9]*Kure National College of Technology, Kure, Hiroshima, 737-8506, Japan*

[10]*Department of Astronomy, Kyoto University, Kitashirakawa-Oiwake-cho, Sakyo-ku, Kyoto 606-8502, Japan*

(Received ; accepted)

Abstract

We present the results of new infrared spectroscopic observations of 37 quasars at $z \sim 3$, selected based on the optical r'-band magnitude and the availability of nearby bright stars for future imaging follow-up with Adaptive Optics system. The supermassive black hole (SMBH) masses ($M_{\rm BH}$) were successfully estimated in 28 out of 37 observed objects from the combination of the Hβ emission linewidth and continuum luminosity at rest-frame 5100 Å. Comparing these results with those from previous studies of quasars with similar redshift, our sample exhibited slightly lower (~ -0.11 dex in median) Eddington ratios; and, the SMBH masses are slightly (~ 0.38 dex in median) higher. The SMBH growth time, $t_{\rm grow}$, was calculated by dividing the estimated SMBH mass by the mass accretion rate measured using optical luminosity. We found, given reasonable assumptions, that $t_{\rm grow}$ was smaller than the age of the

universe at the redshift of individual quasars for a large fraction of observed sources, suggesting that the SMBHs in many of our observed quasars are in growing phase with high accretion rates. A comparison of the SMBH masses derived from our Hβ data and archived C IV data indicated considerable scattering, as indicated in previous studies. All quasars with measured SMBH masses have at least one nearby bright star, such that they are suitable targets for adaptive optics observations to study the mass relationship between SMBHs and host galaxies' stellar component at high redshift.

Key words: galaxies:active – galaxies:nuclei – quasars:supermassive black holes

1. Introduction

The tight correlations between the properties of galaxy spheroidal components (e.g., mass $M_{\rm spheroid}$, velocity dispersion, and luminosity $L_{\rm spheroid}$) and the supermassive black hole (SMBH) mass ($M_{\rm BH}$) in the local universe (Kormendy & Richstone 1995; Marconi & Hunt 2003; McConnell & Ma 2013; see also Kormendy & Ho 2013 for a review) indicate that the formation/growth of galaxies and central SMBHs are closely related (so-called coevolution). Recent multi-wavelength deep surveys have revealed similar downsizing evolution among galaxies, active galactic nuclei (AGNs), and SMBHs in AGNs (Cowie et al. 1996; Kodama et al. 2004; Ueda et al. 2003; Vestergaard et al. 2008), where more luminous, massive galaxies, more luminous AGNs, and more massive active SMBHs in AGNs show their number density peaks at higher redshift. This implies that the histories of cosmic star formation and the mass accretion of SMBHs may be synchronized (Franceschini et al. 1999; Silverman et al. 2008; Zheng et al. 2009). It is important to observationally better constrain how SMBHs and galaxies have coevolved from the early to the current universe.

Depending on various galaxy- and SMBH-growth mechanisms, different redshift (z) evolutions of the $M_{\rm BH}/M_{\rm spheroid}$ ratio ($\equiv R_{\rm BH/spheroid}$) can be predicted. (1) If the outflow from the central SMBH plays a major role in coevolution (Silk & Rees 1998), then the $R_{\rm BH/spheroid}$ ratio is predicted to increase at higher redshift, due to the strong suppression of SMBH accretion at a later age (Wyithe & Loeb 2003). (2) When the SMBH and spheroid growths are governed by major merging of gas-rich galaxies, no significant redshift evolution in $R_{\rm BH/spheroid}$ is expected (e.g., Robertson et al. 2006; see also Kawakatu et al. 2003). (3) If the transformation of disk stars to bulge stars during major mergers is taken into account, in addition to the star formation triggered by mergers, the growth of the $M_{\rm spheroid}$ is enhanced in the late stage, relative to SMBH growth. Hence, the $R_{\rm BH/spheroid}$ ratio is larger at higher redshift, but smaller than (1) (Croton 2006). The differences among models are larger at higher redshift. Therefore, observational investigation of the $R_{\rm BH/spheroid}$ ratio at high redshift is essential to apply constraints

to the coevolution models and/or the allowable parameter ranges of the key processes.

In the local universe, the $M_{\rm BH}$ estimate is obtained via spatially resolved spectroscopy of normal galaxies (e.g., Kuo et al. 2011; van den Bosch & de Zeeuw 2010; Genzel et al. 2010; Walsh et al. 2010; Bender et al. 2005; Cappellari et al. 2002; Miyoshi et al. 1995, see also Kormendy & Ho 2013; Kormendy & Richstone 1995; Genzel et al. 1994 for reviews). However, it is impossible to apply the same method to distant normal galaxies, due to the lack of spatial resolution. Quasars (QSOs; highly luminous AGNs) are useful objects for studying SMBH masses at high redshift, because various strong emission lines from gas clouds, whose dynamics are dominated by the gravitational force of the central SMBHs, can be detected and used to estimate SMBH masses from single epoch spectroscopy, based on the combination of emission linewidths and nearby continuum luminosity (McLure & Jarvis 2002; Vestergaard 2002; Shemmer et al. 2004; Wu et al. 2004; Vestergaard & Peterson 2006; Netzer et al. 2007; Wang et al. 2009; Trakhtenbrot & Netzer 2012).

Previous studies of the $R_{\rm BH/spheroid}$ ratio at high redshift using QSOs were performed mainly at $z < 2$ (e.g., Häring & Rix 2004; Jahnke et al. 2004; Jahnke et al. 2009; Decarli et al. 2010; Merloni et al. 2010; Bennert et al. 2011; Cisternas et al. 2011; Schramm & Silverman 2013; Matsuoka et al. 2014). However, to better distinguish among various coevolution scenarios, data at higher redshift may be preferable. On the other hand, detection of the QSO host galaxy to measure the $M_{\rm spheroid}$ becomes more difficult at higher redshift, because the surface brightness of the host galaxy stellar emission becomes faint in proportion to $(1+z)^4$. Thus, the optimal redshift range must be determined by taking into account the practical observational limitations.

To estimate $M_{\rm BH}$ of distant QSOs at $z > 2$, the C IV λ1549 emission line is commonly used, because it is redshifted into the optical wavelength range, facilitating observation. However, it often shows a large blueshift and an asymmetric profile with respect to low ionization lines (e.g., Gaskell 1982; Tytler & Fan 1992; Richards et al. 2002; Shen et al. 2008, 2011). Therefore, it is not obvious whether or not the C IV linewidths precisely reflect the gravitational potential well of the SMBH. In fact, $M_{\rm BH}$ estimations based on C IV may have large uncertainty, due to the scatter observed in the C IV-derived SMBH mass distribution, compared to the better-calibrated Mg II λ2800- and Hβ λ4861-based SMBH mass estimate (e.g., Baskin & Laor 2005; Netzer et al. 2007; Sulentic et al. 2007; Shen et al. 2008; Marziani & Sulentic 2012). On the other hand, Hβ emission shows a smooth line profile, dominated by the gravitational potential of the SMBH, and is best calibrated to estimate $M_{\rm BH}$ in the local universe, based on the reverberation mapping method (e.g., Peterson & Wandel 1999; Kaspi et al. 2000; Peterson et al. 2004; Bentz et al. 2007, 2009). In this study, the Hβ emission linewidth and nearby continuum luminosity at 5100 Å (L_{5100}) were used to estimate $M_{\rm BH}$ of distant QSOs in the most reliable manner. To cover the redshifted Hβ emission line within the K-band (2.2 μm), the longest high-sensitivity atmospheric window for ground-based

observations, the redshift range of target QSOs was limited to $z < 3.5$. Detection of the QSOs' host galaxy stellar emission at $z \sim 3.5$ was technically feasible using the latest powerful 8–10 m ground-based observation facilities (e.g., Falomo et al. 2005; Peng et al. 2006; Schramm et al. 2008; McLeod & Bechtold 2009; Targett et al. 2011). For these reasons, QSOs at $z < 3.5$ were targeted to constrain their SMBH and galaxy stellar mass ratio, and to observationally better constrain the coevolution of SMBHs and galaxies in the early universe.

In this paper, we report the results of our spectroscopic observations of $z < 3.5$ QSOs for their $M_{\rm BH}$ estimate. The imaging results related to the host galaxies' stellar component will be presented in separate papers (Kawaguchi et al. 2015; in preparation, Saito et al. 2015; in preparation). We describe the sample selection in Section 2 and the observations and data analysis in Section 3. The method used for the $M_{\rm BH}$ estimate is described in detail in Section 4, along with the main results. Section 5 provides a discussion of our main findings, which are summarized in Section 6. Throughout this paper, we adopt the Vega magnitude system for all infrared data and the standard ΛCDM cosmology, with $\Omega_\Lambda = 0.7$, $\Omega_M = 0.3$, and $H_0 = 70\,{\rm km\,s^{-1}\,Mpc^{-1}}$.

2. Observations and Data Analysis

2.1. Sample Selection

All of our samples are radio-quiet QSOs drawn from the seventh data release of the Sloan Digital Sky Survey (SDSS DR7; Abazajian et al. 2009). We first selected QSOs with redshift shown in SDSS DR7 $\sim$ 3.11–3.50, so that the Hβ emission line and 5100 Å continuum could be observed within the K-band. Next, we set limitations on the optical r'-band (0.62 μm) magnitude, $18.5 < r'(SDSS) < 19$. The faint limit was set to obtain sufficient quality spectra for our discussion within a reasonable amount of exposure time. Assuming that observed luminosity cannot exceed the Eddington luminosity limit of $L_{\rm Edd} = 3.2 \times 10^4 (M/M_\odot) L_\odot$, the minimum required $M_{\rm BH}$ is higher for brighter QSOs. The bright limit was set, because observing only the brightest end of the QSOs could strongly bias the data to intrinsically large $M_{\rm BH}$ systems, resulting in a biased view of the $R_{\rm BH/spheroid}$ ratio at high redshift. Radio-loud QSOs were almost excluded because they often show jet-induced extended narrow emission line regions, which could induce considerable uncertainty to the $M_{\rm BH}$ estimate using the emission linewidth. We roughly estimate radio-loudness of our targets from the ratio of their rest-frame luminosities at 5 GHz to those at 2500 Å ($L(5\,{\rm GHz})/L(2500\,{\rm Å})$; Stocke et al. 1992). The $L(2500\,{\rm Å})$ and $L(5\,{\rm GHz})$ are derived from the z'-band magnitude from the SDSS and the 20cm flux from Faint Images of the Radio Sky at Twenty-Centimeters (FIRST) survey (Becker et al. 1994), respectively. Since the wavelength of z'-band and 20 cm correspond to 2500 Å and 5 GHz, respectively, in the rest frame of $z \sim 3$ QSOs, we do not take into account the K correction. Most of our target QSOs (35 out of 37) used in this paper have $L(5\,{\rm GHz})/L(2500\,{\rm Å}) < 10$,

except for 2 target QSOs (J0847+3831 and J1337+3152) with larger radio loudness.

To achieve our final goal for studying the coevolution of SMBH and galaxies at high redshift, adaptive optics (AO) imaging data are going to be used to derive the host galaxy's spheroidal stellar mass, using the Subaru 8.2 m telescope atop Mauna Kea, Hawaii (latitude $\sim +20°$). For AO observation, an AO guide star with $R\,(0.64\,\mu m)$ <18 mag within 60" from the target is required. In addition, to observe each object for longer than 4 hours at a higher elevation than 50° from Mauna Kea, with good AO performance and high spatial resolution, we selected QSOs with declination $-5° < \mathrm{Dec} < +45°$. Finally, to subtract the central bright AGN glare with high accuracy, we chose targets that had at least one nearby PSF reference star with a magnitude similar to that of the target QSOs. Approximately 120 $z \sim 3.5$ QSOs met all of the requirements, among which 37 were chosen for near-infrared spectroscopic observation in this study (Table 1).

2.2. Observations and Data Reduction

The near-infrared K-band (2.2 μm) spectra were obtained using the NASA Infrared Telescope Facility (IRTF 3 m), the United Kingdom Infrared Telescope (UKIRT 3.6 m), the William Herschel Telescope (WHT 4.2 m), and the Subaru Telescope (8.2 m). Bright targets were observed primarily with the SpeX instrument (Rayner et al. 2003) on the IRTF, the UIST (Ramsay et al. 2004) on the UKIRT, and the LIRIS (Manchado et al. 1998) on the WHT. Fainter QSOs were observed with the IRCS instrument (Kobayashi et al. 2000) assisted with the Adaptive Optics system AO188 (Hayano et al. 2010) on the Subaru. With the exception of the Subaru IRCS, these instruments enabled us to obtain H- (1.6 μm) and K-band (2.2 μm) spectra simultaneously. For all targets, Hβ λ4861 and [O III] $\lambda\lambda$4959, 5007 emission lines were observed within the K-band; however, H-band spectra were used when available to better determine the continuum flux level at the shorter part of these emission lines. We also obtained spectroscopic data of standard star (spectral type is A, G, or F) for each target (Table 1) for telluric correction and flux calibration. To estimate the telluric correction, we divided the quasar spectra with standard star spectra, and then multiplied simple blackbody spectra with the temperature corresponding to the spectral type of the standard star derived from Allen's astrophysical quantities (Tokunaga 2000).

2.2.1. IRTF/SpeX

IRTF/SpeX spectra of 20 targets (Table 1) were obtained in the 0.8–2.5 μm cross-dispersed mode with a $1\farcs6 \times 15\farcs0$ slit. This mode provided spectral resolution with $R \sim 375$. Although the R was relatively low comparing to other observations, we choose this mode for safer tracking/guiding and for obtaining better S/N ratios. Spectra were taken at two different positions (A and B) along the slit. Each exposure time ranged from 60–300 s, depending on the magnitude of the targets and the weather conditions. Also, 1–2 coadds were used at each slit position.

The reduction was carried out using the Spectral Extraction Package for SpeX (Spextool; Cushing et al. 2004) that works on IDL. The Spextool goes through almost all data reduction processes, including spectral flat fielding, sky emission subtraction, bad pixel correction, extraction of one-dimensional (1D) spectra, and wavelength calibration (using argon lines). We first created A−B data and then median-combined multiple A−B data sets to increase the S/N ratios. After extraction of a 1D spectrum, the data at the A and B slit positions were summed using the IDL task *xcombspec*. Then the *xtellcor-basic* task in IDL was used for telluric correction and flux calibration. Finally, different order spectra were merged into a single spectrum corresponding to the H- and K-bands (1.41–2.42 μm).

2.2.2. UKIRT/UIST

UKIRT/UIST spectra of five targets (Table 1) were obtained through the $0\farcs6 \times 120\farcs0$ slit with an $H+K$ grism. The achieved spectral resolution is $R \sim 1000$. The spectra were taken at A and B positions along the slit. Each exposure time was 240 s, and 1 coadd was adopted at each position for all targets.

Data were reduced using standard IRAF tasks. Initially, frames taken with an A (or B) beam were subtracted from frames subsequently taken with a B (or A) beam. The resulting subtracted frames were added and divided by a spectroscopic flat image. Then bad pixels and pixels impacted by cosmic rays were replaced with the interpolated values from the surrounding pixels. Finally, the spectra of the QSOs and the standard stars were extracted using the IRAF task *apall*. After wavelength calibration (using argon lines), telluric correction, and flux calibrations, we obtained the final spectra.

2.2.3. WHT/LIRIS

WHT/LIRIS spectra of five targets (Table 1) were taken with the $0\farcs75 \times 252\farcs0$ slit and the $H+K$ grism. The spectral resolution was $R \sim 945$. The exposure time and coadd at each slit position (A or B) were 300 s and 1 coadd, respectively. Data reduction was carried out in the same manner as for UKIRT/UIST.

2.2.4. Subaru/IRCS

Subaru/IRCS spectra of seven targets (Table 1) were obtained using the $0\farcs45 \times 18\farcs0$ slit in the 52-mas mode. We used the K-grism that covers the 1.93–2.48 μm range. The spectral resolution was $R \sim 400$. The exposure time and coadd at each slit position (A and B) were 600 s and 1, respectively. We used IRAF for data reduction similar to that used for UKIRT/UIST and WHT/LIRIS data.

The details of the observations are summarized in Table 1. Redshift and r'-band magnitude are from SDSS catalog. Final spectra are shown in Figures 1 and 2. We also obtained imaging data for all targets and standard stars just before or after spectroscopic observations by using the same instruments used for the spectroscopic observations, and measured photometric magnitudes of the targets. The magnitudes derived from our slit spectra that were calibrated by spectroscopic standard star (possibly affected by slit loss) and those from imaging data gen-

erally agreed within 0.4 mag (Table 2 and Figure 3). We adopted the photometric magnitude from the imaging data for flux calibration.

3. Spectral Analysis

To estimate $M_{\rm BH}$, we fitted the observed spectra with a model combining the linear continuum, the underlying very broad Fe II emission line complex (4500–5600 Å), the broad and narrow Hβ λ4861 emission lines, and two narrow [O III] $\lambda\lambda$4959, 5007 emission lines (as the forbidden [O III] emission line originates primarily from the narrow line regions). The fitting of the spectra of the $z \sim 3$ QSOs was performed individually using QDP (Tennant 1991)[1] and IDL. First, a tentative linear continuum was determined using several data points that were not strongly affected by Hβ, [O III], and Fe II emission lines. For the IRTF, UKIRT, WHT targets, data points at rest-frame 4000–4050 Å or 4150–4200 Å, and 5080–5120 Å were used. For the Subaru targets, because the H-band spectral data were not available, data from rest-frame 4700–4750 Å, 5080–5120 Å, and 5470–5500 Å were adopted. Several data points in the wavelength range considered for continuum determination were significantly affected by the Earth's atmospheric absorption, depending on the redshifts of individual QSOs, and were considerably noisy. Thus, these noisy data points were excluded from the continuum determination.

Next, we fitted the [O III] $\lambda\lambda$4959, 5007 doublet emission lines with two narrow Gaussian components. The linewidth and the redshift of the two components were set to be the same. The relative 5007 Å-to-4959 Å strength was fixed at 3.0 (Dimitrijević et al. 2007). Then the Hβ emission line was fit with two Gaussian (broad and narrow) components. Although some previous studies adopt more complex model (Shemmer et al. 2004; Netzer & Trakhtenbrot 2007; Schulze & Wisotzki 2010), we use only one broad Gaussian and one narrow Gaussian models for Hβ line fitting, because of limited spectral resolution and S/N of our data. For the narrow Hβ emission component, the same linewidth as the [O III] line was adopted. Another Gaussian component with a larger linewidth, corresponding to the broad components of the Hβ emission line, was added. All parameters of this component was set as free parameters. We allowed the velocity shift of the peak wavelength between the narrow Hβ and [O III] lines to be up to 200 km s^{-1}, following Netzer et al. (2007). Then Fe II emission line fitting was carried out using the template derived from the nearby well-studied QSO, I Zw 1, by Tsuzuki et al. (2006). We note that our aim is not to try to accurately fit the Fe II emission features, but to obtain a reliable estimate of the Hβ line width and nearby continuum flux, unaffected by the contamination from the Fe II emission lines. The template was convolved with a Gaussian that had the same linewidth as the broad Hβ emission line, as determined above, because the Fe II emission-line complex originates predominantly from the broad line regions. The fitting

[1] The detailed information is available at http://heasarc.gsfc.nasa.gov/ftools/others/qdp/node3.html.

wavelength ranges for the Fe II features were rest-frame 4500–4650 Å and 5100–5600 Å. Because all QSOs do not have exactly the same Fe II emission line profile as the template used (Fe II spectrum extracted from I Zw 1), we divided the Fe II template into $\lambda < 5008$ Å and $\lambda > 5008$ Å (the Fe II feature shows a minimum value at 5008 Å in the template), and varied their relative strengths to better fit the spectral features actually observed near the Fe II emission in our QSOs spectra. The scaled template was subtracted from the observed spectra. Finally, the Fe II subtracted spectrum was refit using the approach described above. This time, the peak wavelength shift between the narrow Hβ and [O III] was allowed to be up to 450 km s^{-1}. We determined the final fitting parameters for a linear continuum, Hβ, and the [O III] emission lines. The contribution of the instrumental resolution was removed from the fitted linewidth to obtain the actual Hβ emission linewidth.

Some QSOs were fit with only a broad Gaussian component for the Hβ emission line, because the χ^2 values became larger when both broad and narrow Gaussian components were added. For J2134+0011, the Hβ line and [O III] lines were not clearly deblended (Figure 1). Therefore, only wavelengths shorter than 4861 Å were used to fit the broad Hβ emission line. For some sources, continuum fit at the longest wavelength is problematic, because our continuum fitting ranges do not cover longer wavelength part. Also, longer wavelength part of Fe II emission is not well fitted for some sources. However these problematic fit do not affect L_{5100} value significantly.

We succeeded in fitting the Hβ emission lines for 28 out of 37 observed objects. Tables 3 and 4 show the flux and luminosity of Hβ and [O III] emission lines, respectively, based on the above best Gaussian fit. In Table 5, the redshift values estimated from Hβ and [O III] lines are compared to that from the SDSS; they show good agreement.

4. Results

4.1. $M_{\rm BH}$ and $L_{\rm bol}/L_{\rm Edd}$ Estimation

The SMBH mass ($M_{\rm BH}$) of the 28 QSOs (with successful Hβ fit) were estimated from the following formula (Vestergaard & Peterson 2006):

$$\log_{10}(M_{\rm BH}/M_\odot) = \log_{10}\left\{\left[\frac{\rm FWHM(H\beta)}{1000\,\rm km\,s^{-1}}\right]^2\left[\frac{\lambda L_\lambda(5100\,\text{Å})}{10^{44}\,\rm erg\,s^{-1}}\right]^{0.5}\right\} + (6.91 \pm 0.02), \quad (1)$$

and are summarized in Table 6.

We employed a resampling approach to obtain realistic uncertainties of L_{5100}, the full-width at half maximum (FWHM) of the Hβ broad emission line, and $M_{\rm BH}$ (e.g., Schulze & Wisotzki 2010, Assef et al. 2011, Shen & Liu 2012). Namely, we artificially added Gaussian random noise that is scaled by the observed S/N and refit them. We attempted this procedure for 100 simulated spectra for each target. The L_{5100}, FWHM, and $M_{\rm BH}$ error was estimated from the resulting scatter of the derived L_{5100}, FWHM, and $M_{\rm BH}$ values from 100 spectra.

For comparison, we also calculated $M_{\rm BH}$ using the different formula proposed by McLure & Jarvis (2002).

$$\log_{10}(M_{\rm BH}/M_\odot) = \log_{10}\left\{4.74\left[\frac{\rm FWHM(H\beta)}{\rm km\,s^{-1}}\right]^2\left[\frac{\lambda L_\lambda(5100\,\text{Å})}{10^{44}\,\rm erg\,s^{-1}}\right]^{0.61}\right\}. \quad (2)$$

The difference of $M_{\rm BH}$ related to choice of estimator is typically (median) 0.03 dex (range of $-0.36\sim+0.03$ dex). Table 6 and Figure 4 show a comparison of the $M_{\rm BH}$ values derived from both methods, which mutually agree within statistical error.

The AGN bolometric luminosity $L_{\rm bol}$ was calculated from the observed L_{5100} luminosity, using a bolometric correction, $f_L(L_{\rm bol} = f_L \times \lambda \times L_{5100})$. For Type 1 unobscured luminous AGNs, f_L was estimated to be 5–13 (e.g., Elvis et al. 1994; Kaspi et al. 2000; Netzer 2003; Marconi et al. 2004; Richards et al. 2006). We adopt a constant ratio of $f_L = 7$, following Netzer et al. (2007). The AGN bolometric luminosity, relative to the Eddington luminosity for a given $M_{\rm BH}$ ($L_{\rm Edd} = 3.2\times10^4(M_{\rm BH}/M_\odot)L_\odot$), the so-called Eddington ratio ($L_{\rm bol}/L_{\rm Edd}$), is often used to estimate the activity of SMBHs (i.e., the SMBH-mass normalized accretion rate). In the case of $f_L = 7$, the Eddington ratio is given by

$$L_{\rm bol}/L_{\rm Edd} = \frac{7\times\lambda L_{5100}}{1.5\times10^{38}(M_{\rm BH}/M_\odot)}. \quad (3)$$

The estimated $L_{\rm bol}/L_{\rm Edd}$ of 28 QSOs is summarized in Table 6.

4.2. $M_{\rm BH}$ and $L_{\rm bol}/L_{\rm Edd}$ distributions

The upper panels of Figure 5(a) and 5(b) show the distribution of $M_{\rm BH}$ and the Eddington ratio ($L_{\rm bol}/L_{\rm Edd}$) for our sample, respectively. Netzer et al. (2007) and Shemmer et al. (2004) performed near-infrared spectroscopy of QSOs at $z = 2$–4, and measured the SMBH masses in 15 and 29 sources, respectively, based on the Hβ method, of which 14 QSOs in total (8 sources in Netzer's sample, and 6 sources in Shemmer's sample) were at $z > 3$. Our near-infrared spectroscopy tripled the number of $z > 3$ QSOs, with Hβ-based reliably estimated $M_{\rm BH}$ information.

The $M_{\rm BH}$ and $L_{\rm bol}/L_{\rm Edd}$ distributions of these 14 QSOs at $z > 3$ studied by Netzer et al. (2007) and Shemmer et al. (2004) are shown in the lower panels of Figure 5(a) and 5(b), respectively, for comparison. The $M_{\rm BH}$ and $L_{\rm bol}/L_{\rm Edd}$ of the comparison sample are re-calculated using Eq.(1) and (3) with FWHM(Hβ) and L_{5100} drawn from the literature (Table 2 in Netzer et al. (2007), and Table 2 in Shemmer et al. (2004)). The difference of $M_{\rm BH}$ due to choice of estimator (Eq.(1) in this paper and Eq.(1) in Netzer et al. (2007), or Eq.(1) in Shemmer et al. (2004)) is typically 0.25 dex (range of 0.19–0.30 dex) for Netzer's sample and 0.15 dex (range of 0.06–0.23 dex) for Shemmer's sample. The comparison sample has slightly fainter luminosity than our sample (median value of $L_{\rm bol} = 7.88\times10^{46}$ erg s^{-1} for Netzer's sample and $L_{\rm bol} = 1.61\times10^{47}$ erg s^{-1} for our sample), and $M_{\rm BH}$ of the comparison sample is smaller (range of $10^{8.59}$–$10^{9.59}\,M_\odot$) than our sample (range of $10^{8.81}$–$10^{10.13}\,M_\odot$) as shown in

Figure 5(a). On the other hand, the Eddington ratios of our sample are systematically smaller than those of the comparison sample, as shown in Figure 5(b). We performed Kolmogorov-Smirnov test to check if those distributions are statistically the same or not. P-values were calculated to be $P(M_{\rm BH}) = 0.005$ for the $M_{\rm BH}$ distributions, and $P(L_{\rm bol}/L_{\rm Edd}) = 0.045$ for the $L_{\rm bol}/L_{\rm Edd}$ distributions, respectively. The result of K-S test shows that two samples (our sample and the reference sample) are drawn from different parent distributions for both $M_{\rm BH}$ mass distributions and $L_{\rm bol}/L_{\rm Edd}$ distributions (K-S probability of being drawn from the same population < 0.05).

There are two possible reasons to produce the high AGN luminosity, as observed for our QSO sample: (1) the QSO has a modest SMBH mass and a large Eddington ratio, or (2) the QSO has a large SMBH mass and a normal Eddington ratio. If we pick up only the second sample (i.e., QSOs at the higher end of the $M_{\rm BH}$ distribution), $M_{\rm BH}/M_{\rm spheroid}$ ratios could be systematically larger than the typical values (e.g., Lauer et al. 2007; Schulze & Wisotzki 2011, 2014), possibly providing systematically biased results regarding the redshift evolution of the $M_{\rm BH}/M_{\rm spheroid}$ ratios. $M_{\rm BH}$ of our sample and the comparison sample agree within a factor of a few. As shown in Table 6 and Figure 5, it is unlikely that majority of our sample have the $M_{\rm BH}$ much larger than the break (cut-off) of the SMBH mass function at $z = 3.2$ ($\sim 10^{9.7} M_{\odot}$; Kelly & Shen (2013)). The cut-off mass of $\log M_{\rm BH} = 9.7$ was estimated by eye using the mass function at $z = 3.2$ in Figure 4 by Kelly & Shen (2013), although it might be risky to believe the mass function estimated by C IV-based $M_{\rm BH}$ at face values. We compared the Hβ-based and C IV-based $M_{\rm BH}$ (Figure 6, left) and found that C IV-based $M_{\rm BH}$ is not always biased toward large $M_{\rm BH}$. Therefore, we consider that our QSO sample corresponds to the case (1) and that the Lauer-bias is not affecting our sample so severely for a study of redshift evolution of $M_{\rm BH}/M_{\rm spheroid}$. This suggests that we can use our QSO sample to discuss the redshift evolution of the $M_{\rm BH}/M_{\rm spheroid}$ ratios, without obvious strong bias, using the combination of the near-infrared spectroscopy of the $M_{\rm BH}$ estimate (this paper) and ongoing near-infrared, multi-band, high-spatial-resolution AO imaging observations to estimate $M_{\rm spheroid}$. If the local scaling relations hold all the way to $z > 3$, the expected $M_{\rm spheroid}$ for our observed QSOs with $M_{\rm BH} = 6.5 \times 10^8$ – $1.4 \times 10^{10}\, M_{\odot}$, are 4.3×10^{11} – $9.0 \times 10^{12}\, M_{\odot}$, which are detectable with 8 – 10 m telescopes, and have actually been detected in our high-spatial-resolution infrared J- and K'-band imaging observations using Subaru 8.2 m telescope and AO (Kawaguchi et al. 2015; in preparation, Saito et al. 2015; in preparation).

5. Discussion

5.1. Comparison of $M_{\rm BH}$ estimated from Hβ *λ4861 and* C IV *λ*1549

The combination of the C IV λ1549 emission line and continuum luminosity at 1450 Å has often been used to estimate SMBH mass (hereafter, the C IV method) for distant QSOs,

because the C IV emission line is redshifted into the optical wavelength range where spectroscopic observations are easier to attain. However, as mentioned in Section 1, the C IV emission line often shows an asymmetric profile. This suggests that, in addition to the motion dominated by the gravitational potential of SMBH, some other non-gravitational component may be contaminated, such as outflow (Vestergaard & Peterson 2006; Marziani & Sulentic 2012). In fact, several previous studies indicated significant scatter about the comparison of SMBH masses estimated using the Hβ method and the C IV method (e.g., Netzer et al. 2007; Shen et al. 2008; Ho et al. 2012; Shen & Liu 2012; Trakhtenbrot & Netzer 2012).

Shen et al. (2011) reported C IV-based BH masses for our QSO sample, using the following formula (Vestergaard & Peterson 2006):

$$\log_{10}(M_{\rm BH}/M_{\odot}) = \log_{10}\left\{\left[\frac{\rm FWHM(C\,IV)}{1000\,{\rm km\,s^{-1}}}\right]^2\left[\frac{\lambda L_{\lambda}(1350\,\text{Å})}{10^{44}\,{\rm erg\,s^{-1}}}\right]^{0.53}\right\} + (6.66 \pm 0.01). \quad (4)$$

We adopt their estimates to compare with our $M_{\rm BH}$ using the Hβ method. The FWHM of the C IV emission line and C IV-based $M_{\rm BH}$ of our targets are shown in Table 7. For two QSOs, C IV data are not available in Shen et al. (2011). The left panel of Figure 6 shows a comparison between SMBH masses obtained by the two methods for our sample. The scatter is large (0.41 dex) and no significant correlation between Hβ-based and C IV-based $M_{\rm BH}$ is observed. Shen et al. (2008) compared BH masses estimated using different methods for ∼60,000 QSOs at $0.1 \leq z \leq 4.5$, and found that while $M_{\rm BH}$ obtained by the Hβ- and Mg II-methods are tightly correlated, a comparison between C IV-based and Mg II-based $M_{\rm BH}$ shows large scatter with ~ 0.34 dex (see also Shen et al. 2011). Given these results, the large scatter shown in the left panel of Figure 6 for our QSO sample is most likely due to the large uncertainty associated with C IV-based $M_{\rm BH}$. For a reliable $M_{\rm BH}$ estimate for $z \sim 3$ QSOs, the Hβ-method based on near-infrared spectroscopy is preferred over the C IV-method based on optical spectroscopy.

The right panel of Figure 6 is the same plot as that shown in the left panel of Figure 6; however, the marks are distinguished, depending on the Eddington ratio. The samples with high Eddington ratios appear to be distributed slightly to the upper side than those with low Eddington ratios, indicating that the C IV-based $M_{\rm BH}$ was larger than Hβ-based $M_{\rm BH}$ for sources with high Eddington ratios. Figure 7 shows the relationship between the Eddington ratio and the linewidth ratio (FWHM(C IV)/FWHM(Hβ)). A weak correlation is seen log(FWHM(C IV)/FWHM(Hβ))=(0.32±0.15)×log($L_{\rm bol}/L_{\rm Edd}$)+(0.03±0.08) for our sample only or log(FWHM(C IV)/FWHM(Hβ))=(0.35±0.11)×log($L_{\rm bol}/L_{\rm Edd}$)+(0.05±0.06) for all plotted samples. This correlation indicates that objects with a larger Eddington ratio have a wider C IV linewidth, compared to Hβ. QSOs with higher Eddington ratios can have stronger radiation pressure and thereby stronger outflow motion of gas than those with lower Eddington ratios. The C IV line-emitting region is more inside than the Hβ line-emitting region (Peterson & Wandel 1999). It may be possible that this outflow-origin motion broadens the C IV line profile, compared to the SMBH's gravitational motion alone, resulting in a larger $M_{\rm BH}$ estimate

than the Hβ-based method.

5.2. Growth Time of SMBHs

From the AGN bolometric luminosity, we can obtain information on the mass accretion rate. When the measured SMBH mass is divided by the accretion rate, the time scale of SMBH growth can be derived ($t_{\rm grow}$). Following Netzer et al. (2007), we adopt the following formula:

$$t_{\rm grow} = t_{\rm Edd} \frac{\eta/(1-\eta)}{f_L \lambda L_{5100}/L_{\rm Edd}} \ln\left(\frac{M_{\rm BH}}{M_{\rm seed}}\right) \frac{1}{f_{\rm active}}, \quad (5)$$

where t_{Edd} is the Eddington time scale ($= 3.8 \times 10^8$ yr), η is the accretion efficiency, $M_{\rm seed}$ is the seed SMBH mass, $f_{\rm active}$ is the duty cycle (the fractional activity time) of the SMBH, and f_L is the bolometric correction (Section 4.2). We assume fiducial values for $\eta = 0.1$, $M_{\rm seed} = 10^4 M_\odot$, $f_{\rm active} = 1$, and $f_L = 7$, similar to Netzer et al. (2007). We now define $t_{\rm universe}$, which is the age of the universe at the redshift of each QSO (calculated from our adopted cosmology). The $t_{\rm grow}/t_{\rm universe}$ value is summarized in Table 6. Since we have identical choices for $f_{\rm L}$, $M_{\rm seed}$ and $f_{\rm active}$ for all samples, the $t_{\rm growth}$ difference is due to $M_{\rm BH}$ and $L_{\rm bol}/L_{\rm Edd}$. The comparison of these values in our and other samples is shown in Figure 5. For Netzer's and Shemmer's sample, we calculated $t_{\rm grow}/t_{\rm universe}$ value by using Eq.(5) by adopting recalculated $M_{\rm BH}$ and Eddington ratio in Section 4.2. (1) If $t_{\rm grow}/t_{\rm universe} < 1$, then the measured $M_{\rm BH}$ can be reproduced with the estimated mass accretion rate. On the other hand, (2) if $t_{\rm grow}/t_{\rm universe} > 1$, the measured $M_{\rm BH}$ cannot be reproduced with the estimated mass accretion rate, requiring a more active phase in the past at higher redshift than the QSO's redshift. This means that QSOs are not sufficiently active at the QSO redshift. Most of our sample have less than 1 of $t_{\rm grow}/t_{\rm universe}$ values. The range of $t_{\rm grow}/t_{\rm universe}$ values for our sample is 0.22–3.52, and most of our sample have similar value as Netzer et al. (2007) (0.45–2.27). While, QSOs in Shemmer et al. (2004) have systematically smaller $t_{\rm grow}/t_{\rm universe}$ values (0.05–0.16) than ours, which could be due to their sample being selected only from luminous sources ($L \gtrsim 10^{46}\,{\rm erg\,s^{-1}}$). Some of objects, with $t_{\rm grow}/t_{\rm universe} > 1$, in our and Netzer's samples should have experienced a rapidly growing phase in the past, while, Shemmer's sample and most of our sample are in rapidly growing phase at $z \sim 3$.

6. Summary

We present new near-infrared spectroscopic observations of 37 QSOs at $z \sim 3$. We successfully estimated the SMBH masses of 28 out of 37 observed QSOs, using the well-calibrated Hβ-method, based on a broad Hβ emission linewidth and nearby continuum luminosity. A summary of the main results is given below.

1. A comparison of our work to similar studies of $z = 2$–4 QSOs by Netzer et al. (2007) and Shemmer et al. (2004) indicated that our sample had slightly larger $M_{\rm BH}$ and smaller Eddington ratios than the comparison sample. Also, it is unlikely that most of our sample have

the $M_{\rm BH}$ much larger than the break of the BH mass function at that redshift. Given that all our QSOs have at least one nearby bright star, high-spatial-resolution AO observations to investigate the detailed properties of the host galaxies are possible and on-going. Our sample is suited to an investigation of $M_{\rm BH}/M_{\rm spheroid}$ evolution at $z \sim 3$, without obvious selection bias.

2. A comparison of the Hβ-based SMBH mass estimate through near-infrared spectroscopy and previous C IV-based SMBH mass estimates using optical spectroscopy showed large scatter and no significant correlation. QSOs with higher Eddington ratios tended to display higher C IV-derived $M_{\rm BH}$ than Hβ-derived $M_{\rm BH}$, due possibly to effects other than the motion dominated by the gravitational potential of SMBHs. As argued in previous studies, the use of C IV for the $M_{\rm BH}$ estimate could introduce large uncertainty. Hβ-based $M_{\rm BH}$ estimation using near-infrared spectroscopy is desirable for reliable $M_{\rm BH}$ estimates of $z \sim 3$ QSOs.

We appreciate the anonymous referee for his/her useful comment. We are grateful to S. Hayashi for the observation time with the Subaru and K. Imase for supporting observations in the early phase of the study. We wish to thank K. Aoki for general discussions about QSOs, and A. Schulze for helpful discussions about possible bias of our sample. This work was partly supported by the Grants-in-Aid of the Ministry of Education, Science, Culture, and Sport [23540273(MI), 19740105(TK), 09J07156(TM)], and the Grants-in-Aid for Young Scientists [25800099(NK)]. This work was also supported in part by a Japanese Society for the Promotion of Science (JSPS) Core-to-Core Program gInternational Research Network for Dark Energy.h Use of the UKIRT for observations was supported by the National Astronomy Organization of Japan (NAOJ).

References

Abazajian, K. N., et al. 2009, ApJS, 182, 543

Assef, R. J., et al. 2011, ApJ, 742, 93

Baskin, A., & Laor, A. 2005, MNRAS, 356, 1029

Bassani, L., Dadina, M., Maiolino, R., Salvati, M., Risaliti, G., Della Ceca, R., Matt, G., & Zamorani, G. 1999, ApJ, 121, 473

Becker, R. H., White, R. L., & Helfand, D. J. 1994, ASPC, 61, 165

Bell, E. F., & De Jong, R. S. 2001, ApJ, 550, 212

Bender, R., et al. 2005, ApJ, 631, 280

Bennert, V. N., Auger, M. W., Treu, T., Woo, J.-H., & Malkan, M. A. 2011, ApJ, 742, 107

Bentz, M. C., et al. 2007, ApJ, 662, 205

Bentz, M. C., et al. 2009, ApJ, 705, 199

Cappellari, M., Verolme, E. K., van der Marel, R. P., Verdoes Kleijn, G. A., Illingworth, G.D., Franx, M., Carollo, C. M., & de Zeeuw, P. T. 2002, ApJ, 578, 787

Cisternas., M., et al. 2011, ApJ, 741, L11

Cowie, L. L., Songaila, A., Hu, E., & Cohen, J. G. 1996, AJ, 112, 839

Croton, D. J. 2006, MNRAS, 369, 1808

Cushing, M. C., Vacca, W. D., & Rayner J. T. 2004, PASP, 116, 362.

Decarli, R., Falomo, R., Treves, A., Labit, M., Kotilainen, J. K., & Scarpa, R. 2010, MNRAS, 402, 2453

Denney, K. D., et al. 2010, ApJ, 721, 715

Dimitrijević, M. S., Popović, L.Č., Kovačević, J., Dačić, M., & Llić, D. 2007, MNRAS, 374, 1181

Elvis, M., et al. 1994, ApJ, 95, 1

Falomo, R., Kotilainen, J. K., Scarpa, R., & Treves, A. 2005, A&A, 434, 469

Franceschini, A., Hasinger, G., Miyaji, T., & Malquori, D. 1999, MNRAS, 310, L5

Gaskell, C. M. 1982, ApJ, 263, 79

Genzel, R., Hollenbach, D., & Townes, C. H. 1994, Rep. Prog. Phys., 57, 417

Genzel, R., Eisenhauer, F., & Gillessen, S. 2010, Rev. Mod. Phys., 82, 3121

Häring, N., & Rix, H.-W. 2004, ApJ, 604, L89

Hayano, Y., et al. 2010, Proc. SPIE, vol. 7736, 21

Ho, L. C., Goldoni, P., Dong, X-B., Greene, J. E., & Ponti, G. 2012, ApJ, 754, 11

Jahnke, K., et al. 2004, ApJ, 614, 568

Jahnke, K., et al. 2009, ApJ, 706, L215

Kaspi, S., Smith, P. S., Netzer, H., Maoz, D., Jannuzi, B., & Giveon, U. 2000, ApJ, 533, 631

Kawaguchi, T. 2003, ApJ, 593, 69

Kawaguchi,T., Aoki, K., Ohta, K., & Collin, S. 2004, A&A, 420, L23

Kawakatu, N., Umemura, M., & Mori, M. 2003, ApJ, 583, 85

Kelly, C. B., & Shen, Y. 2013, ApJ, 764, 45

Kobayashi, N., et al. 2000, Proc. SPIE, vol. 4008, 1056

Kodama, T., et al. 2004, MNRAS, 350, 1005

Kormendy, J., & Ho, L. C. 2013, ARA&A, 51, 511

Kormendy, J., & Richstone, D. O. 1995, ARA&A, 33, 581
Kuo, C. Y., et al. 2011, ApJ, 727, 20
Lauer, R. T., Tremaine, S., Richstone, D., & Faber, M. S. 2007, ApJ, 670, 249
Magorrian, J., et al. 1998, ApJ, 115, 2285
Manchado, A., et al. 1998, Proc. SPIE, vol. 3354, 448
Marconi, A., & Hunt, L. K. 2003, ApJ, 589, L21
Marconi, A., Risaliti, G., Gilli, R., Hunt, L. K., Maiolino, R., & Salvati, M. 2004, MNRAS, 351, 169
Marziani, P., & Sulentic, J. W. 2012, NewAR, 56, 49
Matsuoka, Y., Strauss, M. A., Price III, T. N., and DiDonato, M. S. 2014, ApJ, 780, 162
McConnell, N, J., & Ma, C-P. 2013, ApJ, 764, 184
McLeod, K. K., & Bechtold, J. 2009, MNRAS, 704, 415
McLure, R. J., & Dunlop, J. S. 2004, MNRAS, 352, 1390
McLure, R. J., & Jarvis, M. J. 2002, MNRAS, 337, 109
Merloni, A., et al. 2010, ApJ, 708, 137
Miyoshi, M., Moran, J., Herrnstein, J., Greenhill, L., Nakai, N., Diamond, P., & Inoue, M. 1995, Nature, 373, 127
Netzer, H. 2003, ApJ, 583, L5
Netzer, H., Lira, P., Trakhtenbrot, B., Shemmer, O., & Cury, I. 2007, ApJ, 671, 1256
Netzer, H., & Trakhtenbrot, B. 2007, ApJ, 654, 763
Peng, C. Y., Impey, C. D., Rix, H-W., Kochanek, C. S., Keeton, C. R., Falco, E. E., Lehár, J., & McLeod, B. A. 2006, ApJ, 649, 616
Peterson, B. M., et al. 2004, ApJ, 613, 682
Peterson, B. M., & Wandel, A. 1999, ApJ, 521, L95
Ramsay, H., et al. 2004, Proc. SPIE, vol. 5492, 1160
Rayner, J. T., et al. 2003, PASP, 115, 362.
Richards, G. T., van den Berk, D. E., Reichard, T. A., Hall, P. B., Schneider, D. P., SubbaRao, M., Thakar, A. R., & York, D. G. 2002, ApJ, 124, 1
Richards, G. T., et al. 2006, ApJ, 166, 470
Robertson, B., Hernquist, L., Cox, T. J., Matteo, T. D., Hopkins, P. F., Martini, P., & Springel, V. 2006, ApJ, 641, 90
Schramm, M., Wisotzki, L., & Jahnke, K. 2008, A&A, 478, 311
Schramm, M., & Silverman, J. D. 2013, ApJ, 767, 13
Schulze, A., & Wisotzki, L. 2010, A&A, 516, A87
Schulze, A., & Wisotzki, L. 2011, A&A, 535, A87
Schulze, A., & Wisotzki, L. 2014, MNRAS, 438, 3422
Shemmer, O., Netzer, H., Maiolino, R., Oliva, E., Croom, S., Corbett, E., & di Fabrizio, L. 2004, ApJ, 614, 547
Shen, Y., Greene, J. E., Strauss, M. A., Richards, G. T., & Schneider, D. P. 2008, ApJ, 680, 169
Shen, Y., et al. 2011, ApJS, 194, 45
Shen, Y., & Liu, X. 2012, ApJ, 753, 125
Silk, J., & Rees, M. J. 1998, A&A, 331, L1

Silverman, J. D., et al. 2008, ApJ, 679, 118
Smith, D. A., & Done, C. 1996, MNRAS, 280, 355
Stocke, J. T., Morris, S. L., Weymann, R. J., & Foltz C. B. 1992, ApJ, 396, 487
Sulentic, J. W., Bachev, R., Marziani, P., Negrete, C. A., & Dultzin, D. 2007, ApJ, 666, 757
Targett, T. A., Dunlop, J. S., McLure, R. J., Best, P. N., Cirasuolo, M., & Almaini, O. 2011, MNRAS, 412, 295
Tokunaga, A. T. 2000, in Allenfs Astrophysical Quantities, 4th ed, ed. A. N. Cox (New York : AIP Press), 143
Trakhtenbrot, B., & Netzer, H. 2012, MNRAS, 427, 3081
Tsuzuki, Y., Kawara, K., Yoshii, Y., Oyabu, S., Tanabe, T., & Matsuoka, Y. 2006, ApJ, 650, 57
Tytler, D., & Fan, X.-M. 1992, ApJS, 79, 1
Ueda, Y., Akiyama, M., Ohta, K., & Miyaji, T. 2003, ApJ, 598, 886
van den Bosch, R. C. E., & de Zeeuw, P. T. 2010, MNRAS, 401, 1770
Vestergaard, M. 2002, ApJ, 571, 733
Vestergaard, M., & Peterson, B. M. 2006, ApJ, 641, 689
Vestergaard, M., Fan, X., Tremonti, C. A., Osmer, P. S., & Richards, G. T. 2008, ApJ, 674, L1
Volonteri, M., & Rees, M. J. 2005, ApJ, 633, 624
Walsh, J. L., Barth, A. J., & Sarzi, M. 2010, ApJ, 721, 762
Wang, J.-G., et al. 2009, ApJ, 707, 1334
Wu, X.-B., Wang, R., Kong, M. Z., Liu, F. K., & Han, J. L. 2004, A&A, 424, 793
Wyithe, J. S. B., & Loeb, A. 2003, ApJ, 595, 614
Zheng, X. Z., et al. 2009, ApJ, 707, 1566

Table 1. Observation log.

(1) Object ID (SDSS J)	(2) z	(3) r' mag	(4) Instrument	(5) Date	(6) Exposure time[sec]	(7) Standard star	(8) Spectral type
014619.97−004628.7	3.17	18.86	IRTF/SpeX	2009 Jan 19, 21	1800+1600	HD13936	A0
031845.17−001845.3	3.22	18.80	WHT/LIRIS	2009 Jan 10	7200	HD15004	A0
072554.52+392243.4	3.25	19.10	Subaru/IRCS	2013 Mar 11	2400	SAO42621	G2
074628.71+301419.0	3.11	18.43	IRTF/SpeX	2009 Jan 19	2120	HD56386	A0
074939.01+433217.6	3.14	18.56	UKIRT/UIST	2009 Jan 20	1920	HD63160	A0
075515.93+154216.6	3.30	19.63	WHT/LIRIS	2009 Jan 10	10500	HD87737	A0
075841.66+174558.0	3.17	18.98	WHT/LIRIS	2010 Mar 3	7200	HR2692	G9
082645.88+071647.0	3.13	18.28	IRTF/SpeX	2009 Jan 20, 21	920+3120	HD65241	A0
083700.82+350550.2	3.31	18.38	UKIRT/UIST	2009 Jan 20	2880	HD71906	A0
084715.16+383110.0	3.18	18.42	UKIRT/UIST	2009 Jan 20	2880	HD63160	A0
094202.04+042244.5	3.28	17.18	IRTF/SpeX	2009 Jan 19	2120	HR3906	A0
095406.40+290208.0	3.24	18.57	IRTF/SpeX	2013 Mar 21	5200	HD91163	G2
095735.37+353520.6	3.27	18.13	IRTF/SpeX	2013 Mar 20	4800	HD77930	F6
100610.55+370513.8	3.20	17.83	IRTF/SpeX	2009 Jan 19	4920	HD88960	A0
103456.31+035859.4	3.36	17.86	IRTF/SpeX	2009 Jan 20	3400	HR3906	A0
111137.72+073305.9	3.46	18.68	WHT/LIRIS	2010 Mar 3	7200	HR4079	F6
111656.89+080829.4	3.23	18.22	IRTF/SpeX	2009 Jan 21	2800	HD97585	A0
113002.35+115438.3	3.39	18.41	UKIRT/UIST	2009 Jan 20	3840	HD101060	A0
114412.77+315800.8	3.23	18.56	UKIRT/UIST	2009 Jan 20	7440	HD98989	A0
123815.03+443026.2	3.25	18.17	IRTF/SpeX	2013 Mar 22	6000	HD111859	F2
133724.69+315254.5	3.18	18.53	IRTF/SpeX	2013 Mar 21	4080	HD121149	G0
133757.87+021820.9	3.33	18.13	IRTF/SpeX	2009 Jan 21, Apr 2	3000+6480	HD124224	A0
140745.50+403702.2	3.20	18.47	IRTF/SpeX	2013 Mar 20	4800	HD134169	G1
142755.85−002951.1	3.36	18.23	IRTF/SpeX	2011 Feb 19	2640	HD116960	A0
150238.38+030228.2	3.35	18.53	IRTF/SpeX	2013 Mar 22	6000	HD34495	F6
150726.32+440649.2	3.12	17.85	IRTF/SpeX	2009 Jan 20	800	HD127304	A0
151044.66+321712.9	3.48	19.83	Subaru/IRCS	2013 Apr 18	2400	HIP81272	F5
155036.80+053749.9	3.15	17.99	IRTF/SpeX	2013 Mar 20	5760	HD145436	F6
155137.22+321307.5	3.18	20.15	Subaru/IRCS	2013 Apr 17	2400	HIP87556	F2
155823.22+353252.2	3.20	19.90	Subaru/IRCS	2013 Apr 19	2400	HIP81272	F5
162508.09+265052.2	3.44	18.92	WHT/LIRIS	2010 Mar 3	6000	HR5728	G2
165523.09+184708.4	3.32	17.81	IRTF/SpeX	2013 Mar 21	4560	HD145228	F0
211936.77+104623.9	3.24	19.19	Subaru/IRCS	2012 Oct 14	3600	HR8041	G1
213023.61+122252.2	3.26	18.04	IRTF/SpeX	2008 Aug 28	4800	HD208108	A0
213455.08+001056.8	3.24	18.77	Subaru/IRCS	2012 Oct 14	3600	HR8041	G1
231858.56−005049.6	3.20	19.56	Subaru/IRCS	2012 Oct 14	3600	HR8041	G1
234150.01+144906.0	3.18	18.44	IRTF/SpeX	2008 Aug 29	8000	BD+14 4774	A0

Notes. Column (1): Object name. Column (2): Sloan Digital Sky Survey (SDSS) redshift. Column (3): SDSS r'-band magnitude (PSF magnitude). Column (4): Used instrument. Column (5): Observation date in UT. Column (6): Exposure time. Column (7): Standard star used for flux calibration and telluric correction. Column (8): Spectral type of the standard star.

Table 2. K-band magnitude.

(1) Object ID (SDSS J)	(2) Spectroscopic Kmag	(3) Imaging Kmag	(4) UKIDSS Kmag	(5) 2MASS Kmag
014619.97−004628.7	16.21	16.69	16.59	–
031845.17−001845.3	16.57	16.38	16.47	–
072554.52+392243.4	17.00	16.95	–	–
074939.01+433217.6	16.24	16.07	–	15.66
075515.93+154216.6	16.53	16.68	–	–
075841.66+174558.0	15.56	16.08	–	–
083700.82+350550.2	16.03	16.06	–	–
084715.16+383110.0	16.07	15.99	–	–
094202.04+042244.5	13.71	14.58	14.58	14.62
095735.37+353520.6	16.31	16.14	–	–
100610.55+370513.8	14.45	15.15	–	15.27
111656.89+080829.4	15.62	15.63	15.56	15.39
113002.35+115438.3	16.19	16.29	16.18	15.98
133724.69+315254.5	16.08	16.15	16.04	–
133757.87+021820.9	15.15	15.74	15.72	>15.17
140745.50+403702.2	14.59	14.48	–	14.63
142755.85−002951.1	14.65	15.49	15.39	15.27
150238.38+030228.2	16.21	16.54	16.15	–
151044.66+321712.9	17.38	17.34	–	–
155036.80+053749.9	15.51	15.76	15.84	>15.59
155137.22+321307.5	18.29	–*	–	–
155823.22+353252.2	17.43	–*	–	–
165523.09+184708.4	15.38	15.43	–	–
211936.77+104623.9	16.88	16.84	–	–
213023.61+122252.2	15.06	–*	–	15.29
213455.08+001056.8	16.72	16.97	16.69	–
231858.56−005049.6	16.85	17.09	16.95	–
234150.01+144906.0	16.15	15.87	15.92	–

Notes. Column (1): Object name. Column (2): Spectroscopic magnitude based on our data. Flux calibration is carried out by using spectroscopic standard star. Column (3): Imaging magnitude based on our data (PSF magnitude). Column (4): UKIDSS magnitude (aperture magnitude). Column (5): 2MASS magnitude (PSF magnitude). Only sources whose SMBH masses ($M_{\rm BH}$) were estimated are listed. Imaging magnitudes were used for flux calibration.

* Imaging data quality is not good enough to obtain reliable photometric magnitude.

Table 3. 5100Å continuum flux densities and Hβ flux and luminosity.

(1)	(2)	Flux [10^{-15}erg/s/cm^2]		Luminosity [10^{44}erg/s]	
Object ID (SDSS J)	5100Å continuum flux	(3)	(4)	(5)	(6)
	[10^{-17}erg/s/cm^2/Å]	Hβ broad	Hβ narrow	Hβ broad	Hβ narrow
014619.97−004628.7	0.860 ± 0.047	0.661 ± 0.097	0.065 ± 0.025	0.584 ± 0.086	0.057 ± 0.022
031845.17−001845.3	0.727 ± 0.121	1.270 ± 0.144	–	1.164 ± 0.132	–
072554.52+392243.4	0.631 ± 0.014	0.415 ± 0.016	–	0.386 ± 0.015	–
074939.01+433217.6	1.278 ± 0.064	1.033 ± 0.116	0.075 ± 0.045	0.891 ± 0.100	0.065 ± 0.039
075515.93+154216.6	0.690 ± 0.151	0.216 ± 0.085	–	0.210 ± 0.083	–
075841.66+174558.0	0.932 ± 0.087	0.857 ± 0.012	–	0.757 ± 0.107	–
083700.82+350550.2	1.268 ± 0.093	0.922 ± 0.148	0.078 ± 0.070	0.903 ± 0.145	0.077 ± 0.069
084715.16+383110.0	1.405 ± 0.061	1.017 ± 0.059	–	0.905 ± 0.053	–
094202.04+042244.5	5.473 ± 0.110	2.900 ± 0.179	0.435 ± 0.064	2.779 ± 0.171	0.417 ± 0.061
095735.37+353520.6	1.354 ± 0.034	0.497 ± 0.029	–	0.473 ± 0.028	–
100610.55+370513.8	3.223 ± 0.043	1.383 ± 0.144	0.148 ± 0.048	1.250 ± 0.130	0.134 ± 0.043
111656.89+080829.4	2.692 ± 0.119	2.235 ± 0.174	0.109 ± 0.053	2.064 ± 0.160	0.101 ± 0.049
113002.35+115438.3	0.981 ± 0.065	0.559 ± 0.059	0.062 ± 0.028	0.580 ± 0.061	0.064 ± 0.029
133724.69+315254.5	1.163 ± 0.025	0.887 ± 0.056	0.448 ± 0.030	0.789 ± 0.050	0.399 ± 0.027
133757.87+021820.9	1.601 ± 0.079	0.790 ± 0.114	0.194 ± 0.066	0.785 ± 0.113	0.193 ± 0.066
140745.50+403702.2	7.128 ± 0.031	2.378 ± 0.050	–	2.148 ± 0.045	–
142755.85−002951.1	2.274 ± 0.082	1.240 ± 0.018	0.370 ± 0.057	1.259 ± 0.181	0.376 ± 0.058
150238.38+030228.2	0.665 ± 0.030	0.644 ± 0.031	–	0.649 ± 0.031	–
151044.66+321712.9	0.265 ± 0.016	0.295 ± 0.028	–	0.325 ± 0.031	–
155036.80+053749.9	1.793 ± 0.032	1.203 ± 0.046	0.242 ± 0.015	1.046 ± 0.040	0.210 ± 0.013
155137.22+321307.5	0.506 ± 0.035	0.487 ± 0.105	0.102 ± 0.024	0.434 ± 0.093	0.090 ± 0.021
155823.22+353252.2	0.413 ± 0.019	0.243 ± 0.116	0.047 ± 0.014	0.219 ± 0.105	0.042 ± 0.013
165523.09+184708.4	2.388 ± 0.039	0.691 ± 0.047	0.331 ± 0.031	0.682 ± 0.046	0.326 ± 0.031
211936.77+104623.9	0.684 ± 0.015	0.229 ± 0.059	0.115 ± 0.050	0.213 ± 0.055	0.107 ± 0.046
213023.61+122252.2	3.620 ± 0.117	1.692 ± 0.139	0.321 ± 0.040	1.597 ± 0.131	0.303 ± 0.038
213455.08+001056.8	0.664 ± 0.015	0.169 ± 0.017	–	0.157 ± 0.016	–
231858.56−005049.6	0.567 ± 0.015	0.189 ± 0.028	0.040 ± 0.018	0.171 ± 0.025	0.036 ± 0.016
234150.01+144906.0	1.891 ± 0.046	0.604 ± 0.072	–	0.537 ± 0.064	–

Notes. Column (1): Object name. Column (2): Continuum flux at 5100Å (3): Flux of broad Hβ emission line. Column (4): Flux of narrow Hβ emission line. Column (5): Luminosity of broad Hβ emission line. Column (6): Luminosity of narrow Hβ emission line. The values were calculated from fitting results.

Table 4. [O III] flux and luminosity.

	Flux [10^{-15}erg/s/cm^2]		Luminosity [10^{44}erg/s]	
(1)	(2)	(3)	(4)	(5)
Object ID (SDSS J)	[O III] λ5007	[O III] λ4959	[O III] λ5007	[O III] λ4959
014619.97−004628.7	0.361 ± 0.016	0.120 ± 0.005	0.318 ± 0.014	0.106 ± 0.005
031845.17−001845.3	0.351 ± 0.084	0.117 ± 0.028	0.322 ± 0.078	0.107 ± 0.026
072554.52+392243.4	0.170 ± 0.016	0.057 ± 0.005	0.158 ± 0.015	0.053 ± 0.005
074939.01+433217.6	1.127 ± 0.040	0.376 ± 0.013	0.973 ± 0.035	0.324 ± 0.012
075515.93+154216.6	0.185 ± 0.161	0.062 ± 0.054	0.180 ± 0.156	0.060 ± 0.052
075841.66+174558.0	0.922 ± 0.098	0.307 ± 0.033	0.814 ± 0.087	0.271 ± 0.029
083700.82+350550.2	0.422 ± 0.094	0.141 ± 0.031	0.413 ± 0.092	0.138 ± 0.031
084715.16+383110.0	0.755 ± 0.031	0.252 ± 0.010	0.672 ± 0.027	0.224 ± 0.009
094202.04+042244.5	1.137 ± 0.063	0.379 ± 0.021	1.090 ± 0.060	0.363 ± 0.020
095735.37+353520.6	0.173 ± 0.030	0.058 ± 0.010	0.165 ± 0.028	0.055 ± 0.009
100610.55+370513.8	1.171 ± 0.046	0.390 ± 0.015	1.058 ± 0.041	0.353 ± 0.014
111656.89+080829.4	0.765 ± 0.058	0.255 ± 0.019	0.707 ± 0.053	0.236 ± 0.018
113002.35+115438.3	0.212 ± 0.038	0.071 ± 0.013	0.219 ± 0.039	0.073 ± 0.013
133724.69+315254.5	0.462 ± 0.022	0.154 ± 0.007	0.411 ± 0.020	0.137 ± 0.007
133757.87+021820.9	0.436 ± 0.061	0.145 ± 0.020	0.433 ± 0.061	0.014 ± 0.020
140745.50+403702.2	–	–	–	–
142755.85−002951.1	0.507 ± 0.050	0.169 ± 0.017	0.514 ± 0.050	0.171 ± 0.017
150238.38+030228.2	–	–	–	–
151044.66+321712.9	–	–	–	–
155036.80+053749.9	0.993 ± 0.017	0.331 ± 0.006	0.864 ± 0.015	0.288 ± 0.005
155137.22+321307.5	0.416 ± 0.027	0.139 ± 0.009	0.370 ± 0.024	0.123 ± 0.008
155823.22+353252.2	0.110 ± 0.017	0.037 ± 0.006	0.099 ± 0.015	0.033 ± 0.005
165523.09+184708.4	0.534 ± 0.028	0.178 ± 0.009	0.527 ± 0.027	0.176 ± 0.009
211936.77+104623.9	0.159 ± 0.024	0.053 ± 0.008	0.148 ± 0.022	0.049 ± 0.007
213023.61+122252.2	1.535 ± 0.051	0.512 ± 0.017	1.449 ± 0.048	0.483 ± 0.016
213455.08+001056.8	–	–	–	–
231858.56−005049.6	0.049 ± 0.018	0.016 ± 0.006	0.044 ± 0.016	0.015 ± 0.005
234150.01+144906.0	0.013 ± 0.005	0.004 ± 0.002	0.111 ± 0.046	0.037 ± 0.015

Notes. Column (1): Object name. Column (2): Flux of [O III]λ5007 emission line. Column (3): Flux of [O III]λ4959 emission line. Column (4): Luminosity of [O III]λ5007 emission line. Column (5): Luminosity of [O III]λ4959 emission line. The values were calculated from fitting results.

Table 5. Redshift comparison.

(1)	(2)	(3)	(4)
Object ID (SDSS J)	Hβ	[O III] λ5007	SDSS
014619.97−004628.7	3.173	3.170	3.173
031845.17−001845.3	3.225	3.222	3.224
072554.52+392243.4	3.258	3.251	3.249
074939.01+433217.6	3.144	3.134	3.141
075515.93+154216.6	3.288	3.294	3.298
075841.66+174558.0	3.182	3.166	3.170
083700.82+350550.2	3.322	3.305	3.311
084715.16+383110.0	3.189	3.184	3.180
094202.04+042244.5	3.287	3.277	3.276
095735.37+353520.6	3.287	3.269	3.276
100610.55+370513.8	3.203	3.201	3.201
111656.89+080829.4	3.240	3.239	3.234
113002.35+115438.3	3.434	3.392	3.394
133724.69+315254.5	3.192	3.175	3.208
133757.87+021820.9	3.358	3.334	3.333
140745.50+403702.2	3.168	–	3.200
142755.85−002951.1	3.373	3.362	3.365
150238.38+030228.2	3.370	–	3.358
151044.66+321712.9	3.478	–	3.474
155036.80+053749.9	3.159	3.147	3.153
155137.22+321307.5	3.143	3.152	3.184
155823.22+353252.2	3.191	3.186	3.198
165523.09+184708.4	3.375	3.349	3.323
211936.77+104623.9	3.274	3.257	3.248
213023.61+122252.2	3.267	3.274	3.272
213455.08+001056.8	3.289	–	3.289
231858.56−005049.6	3.211	3.208	3.209
234150.01+144906.0	3.170	3.181	3.184

Notes. Column (1): Object name. Column (2): Redshift measured by broad Hβ emission line. Column (3): Redshift measured by [O III]λ5007 emission line. Column (4): SDSS redshift.

Table 6. Observed and derived properties related to SMBHs.

(1) Object ID (SDSS J)	(2) FWHM(Hβ)[10^3km/s]	(3) λL_λ(5100Å)[10^{46}erg/s]	(4) log $M_{\rm BH}[M_\odot]$	(5) log $L_{\rm bol}/L_{\rm Edd}$	(6) $t_{\rm grow}/t_{\rm universe}$	(7) log $M_{\rm BH}[M_\odot]$ McL
014619.97−004628.7	6.92 ± 1.30	1.61 ± 0.09	9.68 ± 0.17	−0.804	1.76	9.69 ± 0.17
031845.17−001845.3	4.79 ± 0.48	1.43 ± 0.24	9.34 ± 0.09	−0.516	0.87	9.34 ± 0.09
072554.52+392243.4	4.32 ± 0.41	1.27 ± 0.03	9.23 ± 0.08	−0.457	0.76	9.23 ± 0.08
074939.01+433217.6	7.14 ± 0.53	2.33 ± 0.12	9.80 ± 0.06	−0.764	1.63	9.82 ± 0.06
075515.93+154216.6	2.70 ± 0.80	1.47 ± 0.32	8.81 ± 0.28	0.026	0.23	8.81 ± 0.28
075841.66+174558.0	4.64 ± 1.03	1.75 ± 0.16	9.34 ± 0.20	−0.428	0.70	9.35 ± 0.20
083700.82+350550.2	5.18 ± 0.53	2.73 ± 0.20	9.55 ± 0.09	−0.445	0.80	9.59 ± 0.09
084715.16+383110.0	4.29 ± 0.46	2.67 ± 0.12	9.38 ± 0.09	−0.284	0.51	9.41 ± 0.09
094202.04+042244.5	5.34 ± 0.22	11.45 ± 0.23	9.89 ± 0.03	−0.162	0.44	10.00 ± 0.03
095735.37+353520.6	6.07 ± 0.71	2.80 ± 0.07	9.69 ± 0.11	−0.574	1.08	9.73 ± 0.11
100610.55+370513.8	5.94 ± 0.40	6.23 ± 0.08	9.85 ± 0.06	−0.387	0.71	9.93 ± 0.06
111656.89+080829.4	3.34 ± 0.22	5.36 ± 0.24	9.32 ± 0.05	0.078	0.22	9.39 ± 0.05
113002.35+115438.3	6.05 ± 0.42	2.28 ± 0.15	9.65 ± 0.06	−0.623	1.26	9.67 ± 0.06
133724.69+315254.5	5.73 ± 0.24	2.21 ± 0.05	9.60 ± 0.04	−0.587	1.06	9.62 ± 0.04
133757.87+021820.9	5.18 ± 1.09	3.51 ± 0.17	9.59 ± 0.22	−0.376	0.69	9.63 ± 0.22
140745.50+403702.2	6.72 ± 0.17	13.79 ± 0.06	10.13 ± 0.02	−0.389	0.74	10.24 ± 0.02
142755.85−002951.1	5.49 ± 0.87	5.13 ± 0.19	9.73 ± 0.13	−0.351	0.73	9.80 ± 0.13
150238.38+030228.2	5.28 ± 0.21	1.49 ± 0.07	9.44 ± 0.03	−0.598	1.13	9.45 ± 0.03
151044.66+321712.9	5.04 ± 0.60	0.67 ± 0.04	9.22 ± 0.10	−0.725	1.51	9.19 ± 0.10
155036.80+053749.9	6.11 ± 0.29	3.30 ± 0.06	9.74 ± 0.04	−0.552	1.00	9.78 ± 0.04
155137.22+321307.5	6.70 ± 1.12	0.96 ± 0.07	9.54 ± 0.18	−0.889	2.11	9.52 ± 0.18
155823.22+353252.2	8.49 ± 2.98	0.80 ± 0.04	9.67 ± 0.28	−1.098	3.52	9.65 ± 0.28
165523.09+184708.4	5.93 ± 0.21	5.19 ± 0.08	9.81 ± 0.03	−0.426	0.80	9.88 ± 0.03
211936.77+104623.9	4.72 ± 0.78	1.38 ± 0.03	9.31 ± 0.16	−0.501	0.85	9.31 ± 0.16
213023.61+122252.2	4.39 ± 0.35	7.43 ± 0.24	9.63 ± 0.07	−0.090	0.35	9.71 ± 0.06
213455.08+001056.8	>3.09 ± 0.31*	1.34 ± 0.03	>8.95 ± 0.09	< −0.157	>0.36	>8.95 ± 0.08
231858.56−005049.6	5.21 ± 0.75	1.10 ± 0.03	9.35 ± 0.13	−0.650	1.19	9.35 ± 0.13
234150.01+144906.0	7.49 ± 4.36	3.59 ± 0.09	9.72 ± 0.69	−0.496	0.88	9.77 ± 0.69

Notes. Column (1): Object name. Column (2): Full-width at half maximum (FWHM) of broad Hβ emission line. Column (3): Continuum luminosity at 5100 Å. Column (4): Decimal logarithm of SMBH mass. Statistical errors were estimated by resampling approach (Section 4.1; Schulze & Wisotzki 2010, Assef et al. 2011, Shen & Liu 2012). Column (5): Decimal logarithm of Eddington ratio. Column (6): Ratio of SMBH growth time ($t_{\rm grow}$) and the age of the universe ($t_{\rm universe}$). $t_{\rm grow}$ is the time scale of SMBH growth, calculated using the measured $M_{\rm BH}$ and the Eddington ratio. $t_{\rm universe}$ is dependent on the redshift of each target. See Section 5.2 for more details. Column (7): Decimal logarithm of SMBH masses derived from the formula in McLure & Jarvis (2002).

* For this object, we cannot measure the [O III] emission linewidth, therefore, the Hβ narrow component is not subtracted. If the Hβ narrow component exists, then the Hβ broad emission linewidth broadens and the estimated $M_{\rm BH}$ becomes larger.

Table 7. C IV-based SMBH mass in our QSO sample.

(1)	(2)	(3)
Object ID (SDSS J)	FWHM(C IV)[10^3km/s]	log $M_{\rm BH}[M_\odot]$
014619.97−004628.7	2.70 ± 0.15	8.91 ± 0.05
031845.17−001845.3	3.96 ± 0.14	9.25 ± 0.03
072554.52+392243.4	3.39 ± 0.18	9.11 ± 0.05
074939.01+433217.6	2.52 ± 0.07	8.92 ± 0.03
075515.93+154216.6	2.87 ± 0.24	8.78 ± 0.07
075841.66+174558.0	3.37 ± 0.11	9.04 ± 0.03
083700.82+350550.2	3.89 ± 0.30	9.36 ± 0.07
084715.16+383110.0	2.25 ± 0.11	8.87 ± 0.04
094202.04+042244.5	3.32 ± 0.10	9.49 ± 0.03
095735.37+353520.6	7.56 ± 0.55	9.96 ± 0.06
100610.55+370513.8	4.23 ± 0.11	9.42 ± 0.02
111656.89+080829.4	2.81 ± 0.20	9.07 ± 0.06
113002.35+115438.3	6.28 ± 1.38	9.76 ± 0.19
133724.69+315254.5	4.03 ± 0.33	9.34 ± 0.07
133757.87+021820.9	7.39 ± 0.41	9.96 ± 0.03
140745.50+403702.2	4.54 ± 1.75	9.41 ± 0.34
142755.85−002951.1	3.04 ± 0.06	9.20 ± 0.02
150238.38+030228.2	6.45 ± 0.70	9.80 ± 0.09
151044.66+321712.9	5.84 ± 0.61	9.44 ± 0.09
155036.80+053749.9	2.76 ± 0.09	9.12 ± 0.03
155137.22+321307.5	–*	–
155823.22+353252.2	2.05 ± 0.08	8.43 ± 0.04
165523.09+184708.4	9.56 ± 0.59	10.32 ± 0.05
211936.77+104623.9	5.63 ± 0.26	9.53 ± 0.04
213023.61+122252.2	2.52 ± 0.10	9.11 ± 0.03
213455.08+001056.8	6.10 ± 0.41	9.66 ± 0.06
231858.56−005049.6	3.21 ± 0.37	8.87 ± 0.10
234150.01+144906.0	–*	–

Notes. Column (1): Object name. Column (2): FWHM of C IV emission line from SDSS (Shen et al. 2011). Column (3): C IV-based SMBH mass from SDSS (Shen et al. 2011).

* For these objects, C IV data are not available in Shen et al. (2011).

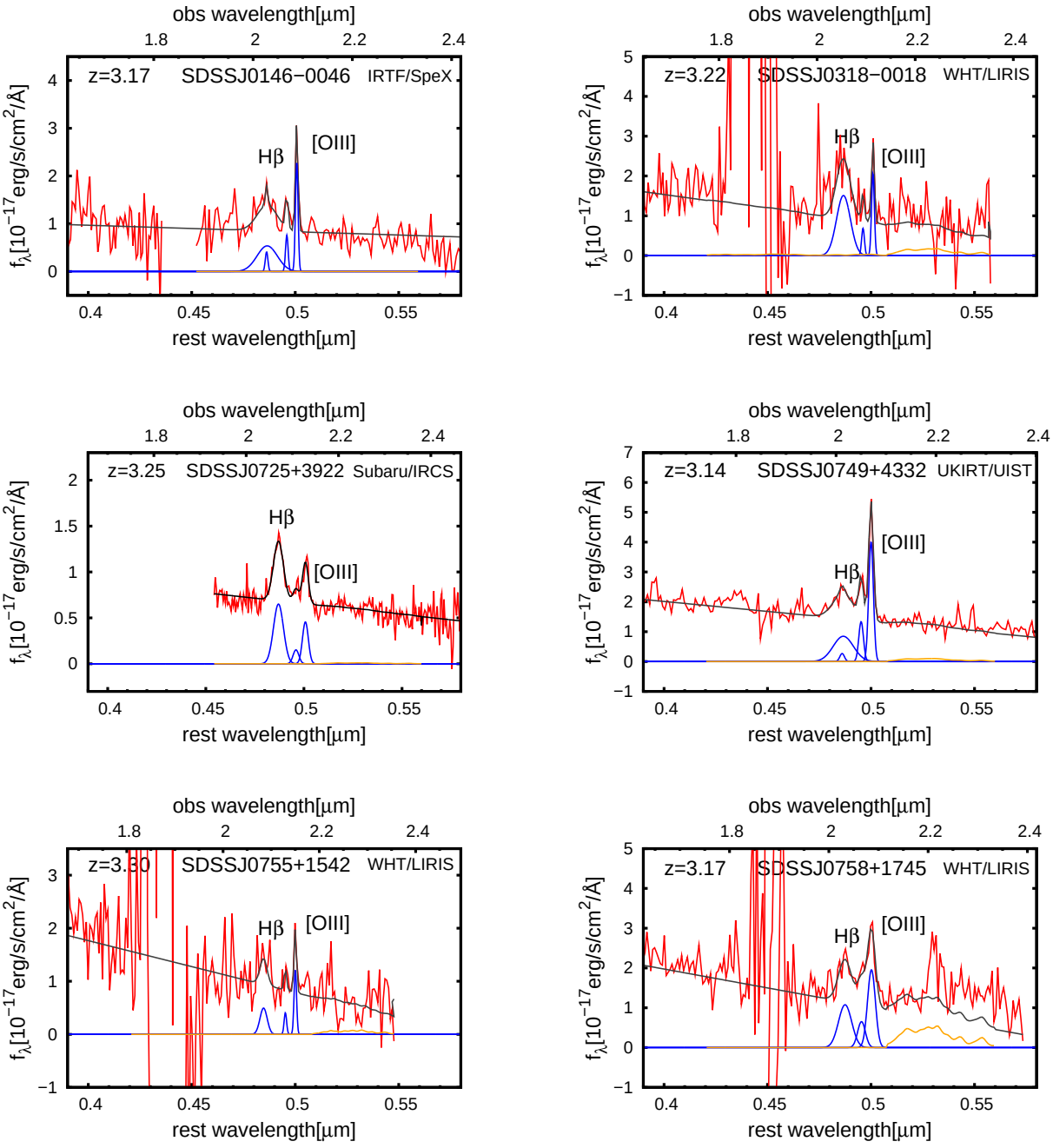

Fig. 1. All spectra of 28 $z \sim 3$ QSOs with fitted Hβ and the [O III] emission lines in our sample. The abscissa is the rest-frame (bottom) and the observed (top) wavelength in [μm]. The ordinate is the flux in [10^{-17}erg/s/cm^2/Å]. The best-fit model (black line) in each panel is composed of a continuum component, Fe II emission (orange line), and Hβ and [O III] emission lines (blue lines).

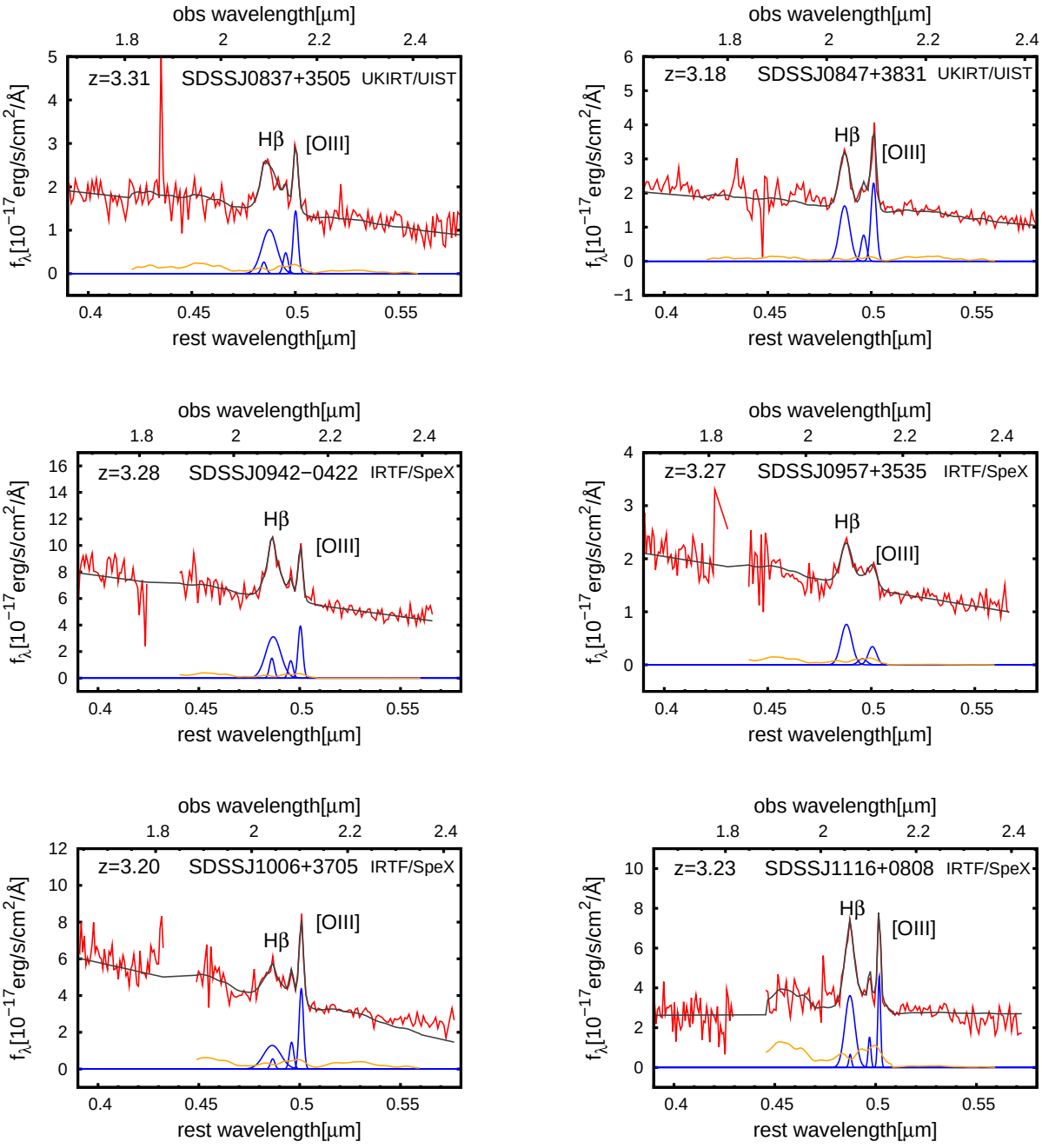

Fig. 1. continued

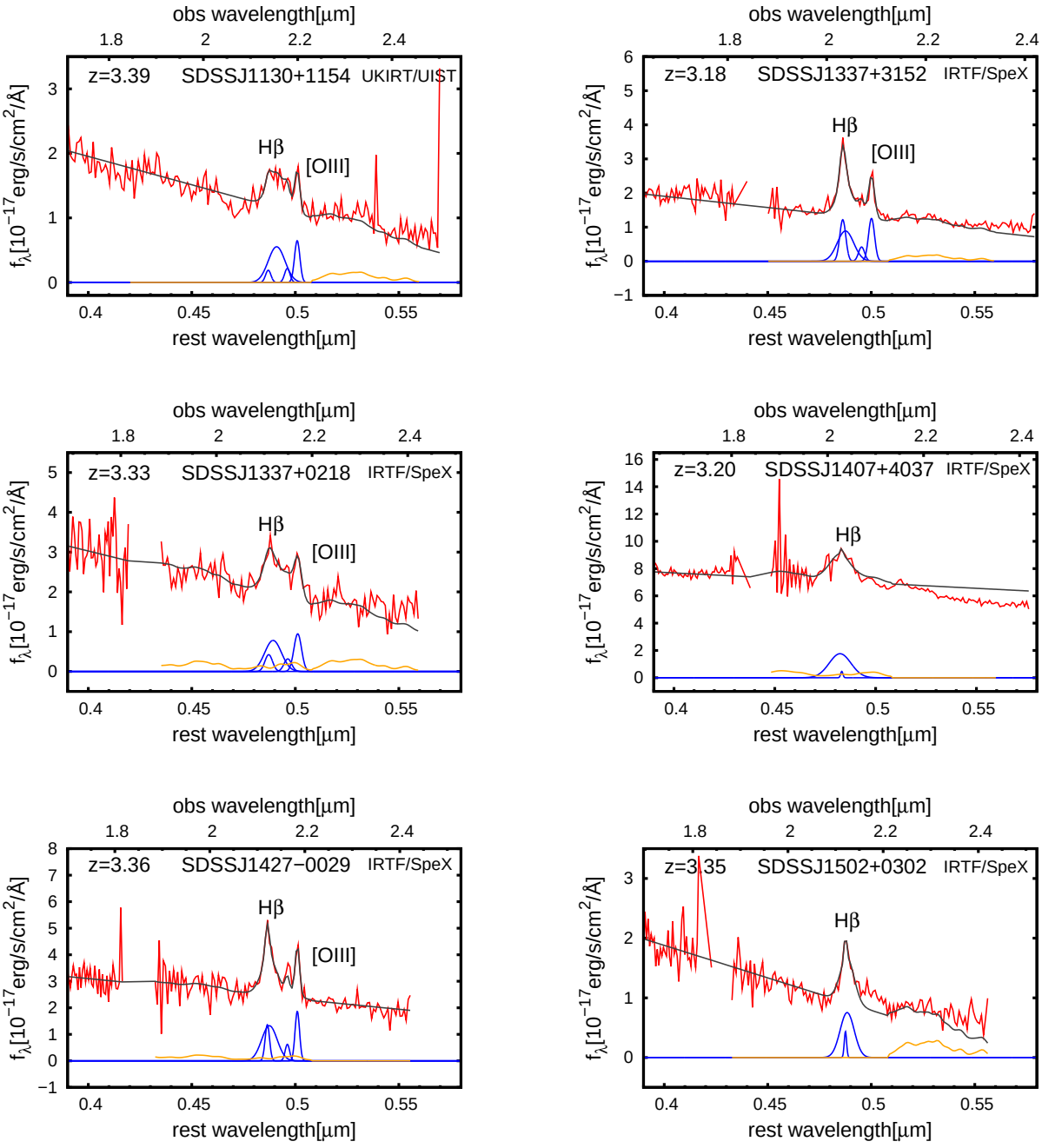

Fig. 1. continued

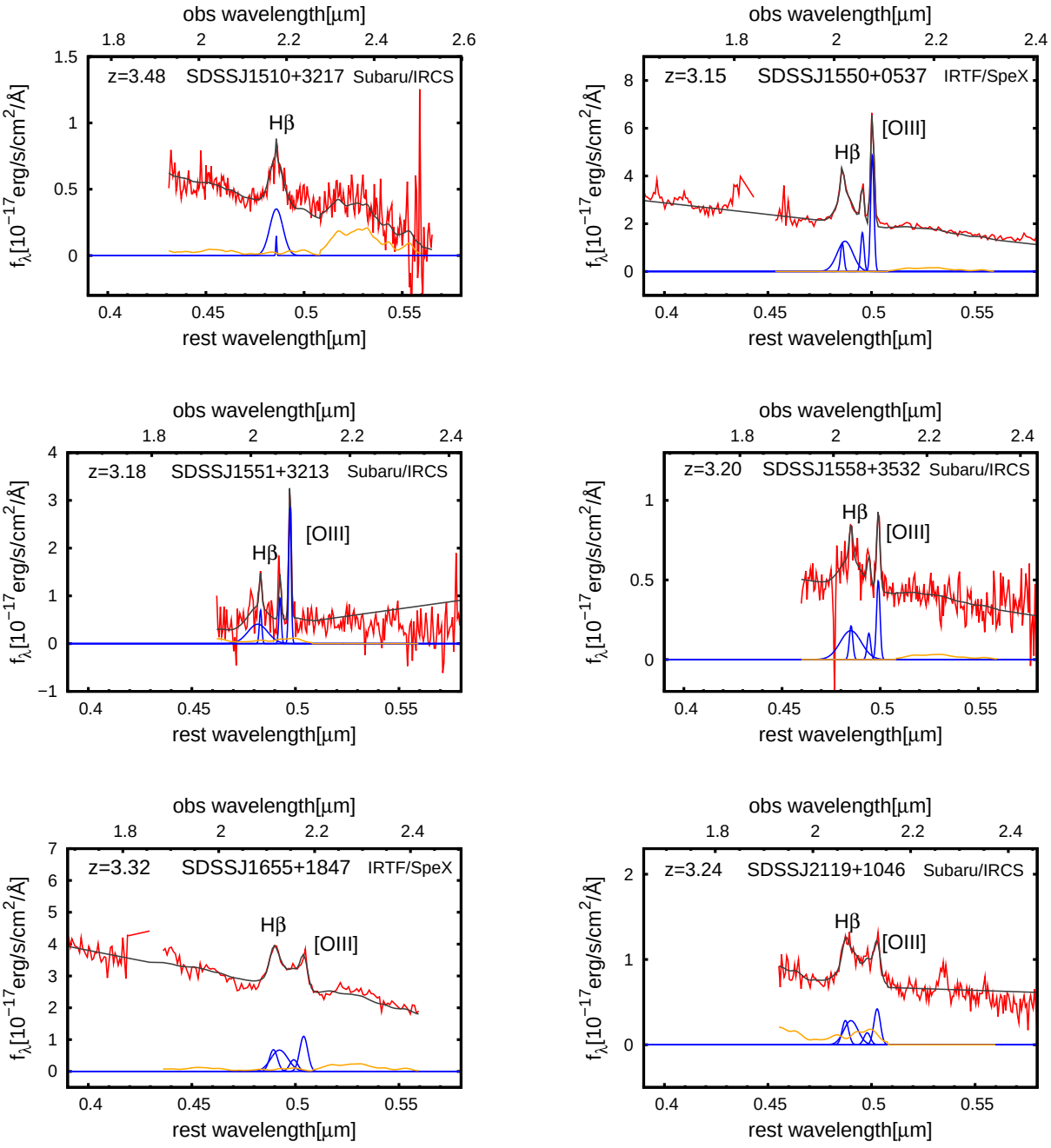

Fig. 1. continued

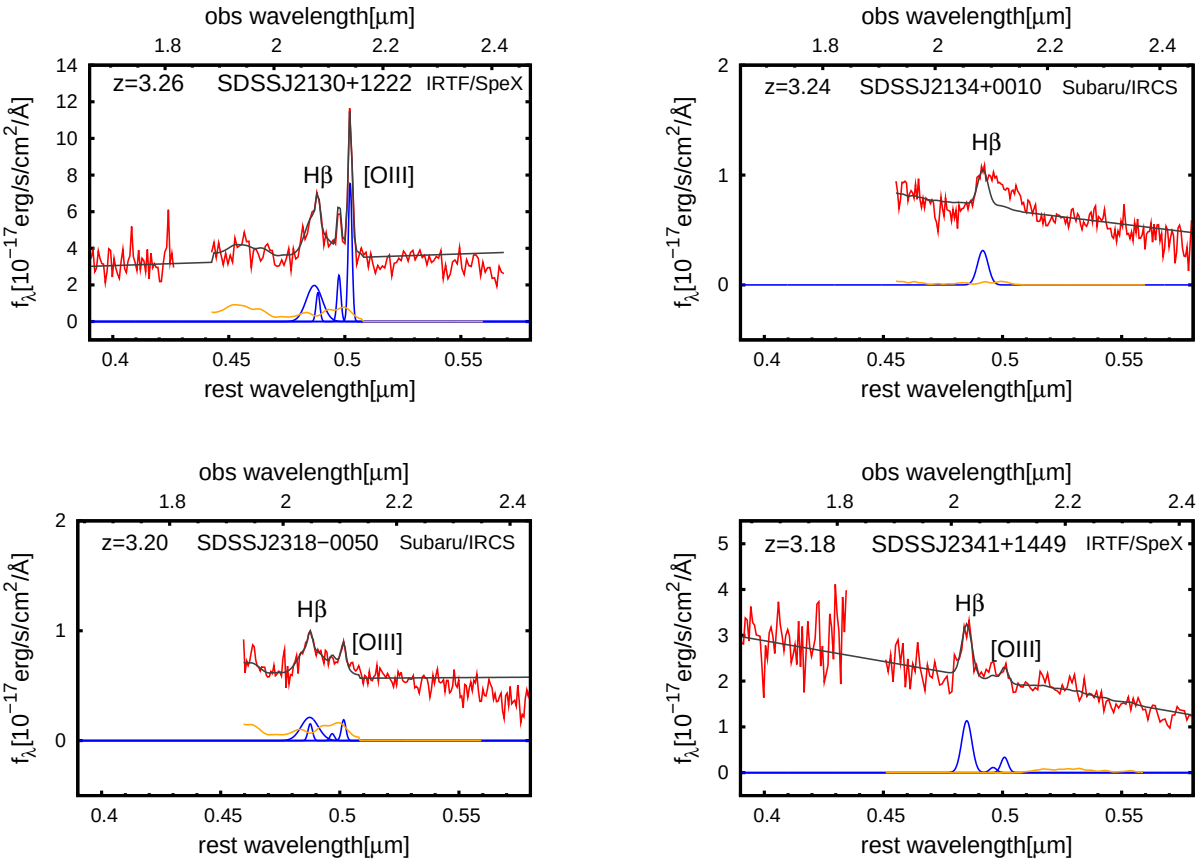

Fig. 1. continued

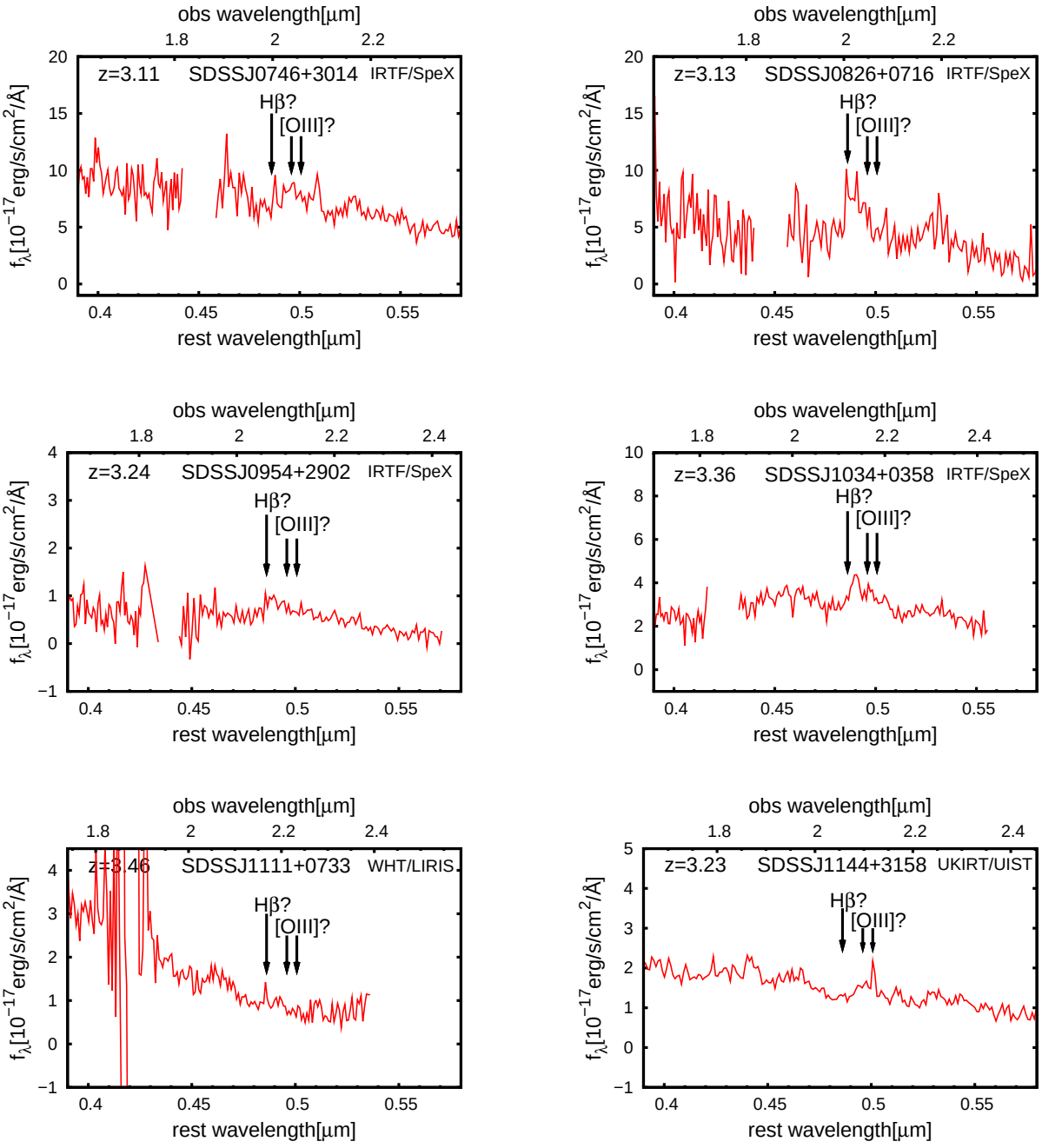

Fig. 2. Spectra without clearly detected emission lines. The abscissa is the rest frame (bottom) and the observed (top) wavelength in [μm]. The ordinate is the flux in [10^{-17}erg/s/cm^2/Å]. Hβ and [O III] emission lines should be positioned as indicated by the downward arrows in each panel.

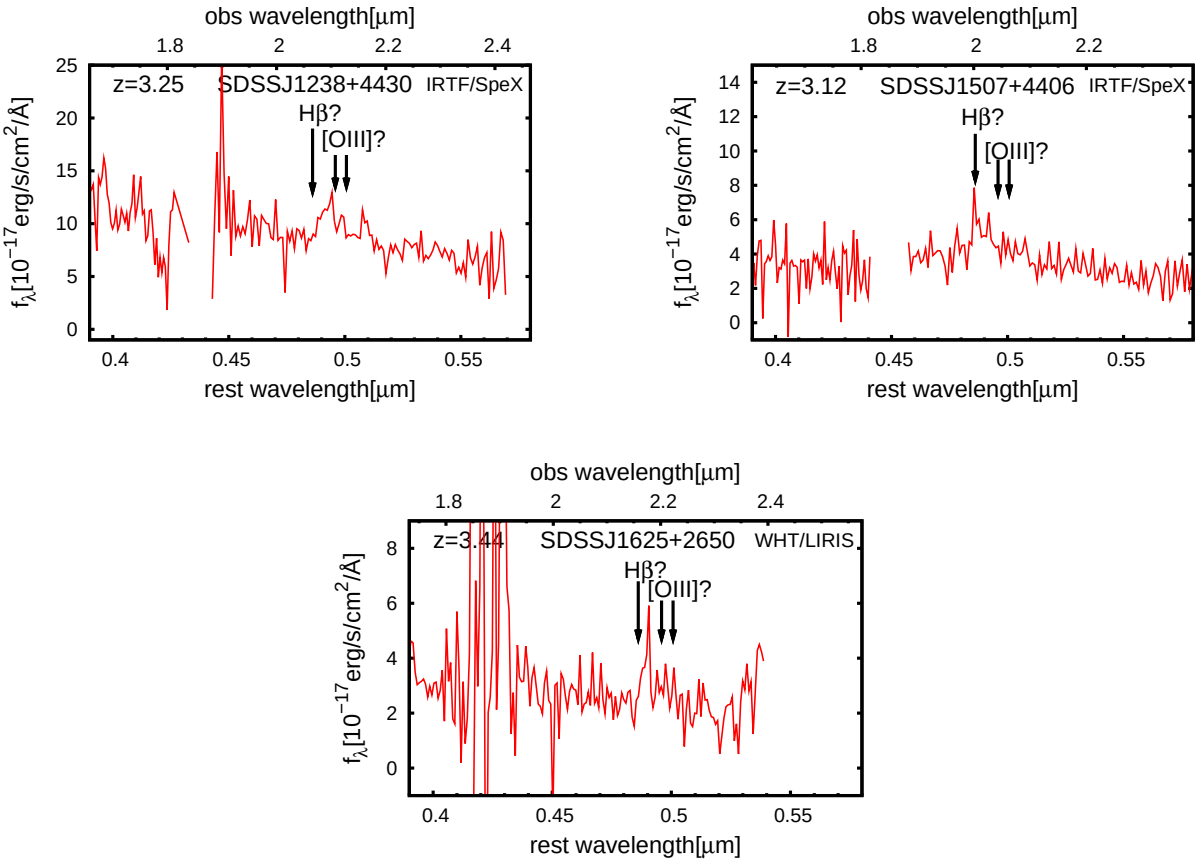

Fig. 2. continued

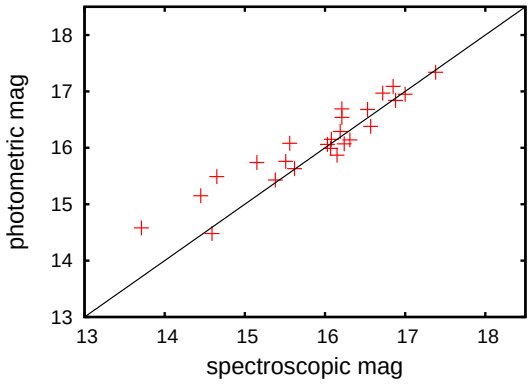

Fig. 3. Comparison of K-band magnitudes estimated using spectroscopic data (abscissa) and imaging data (ordinate). The dashed line represents a 1:1 correspondence.

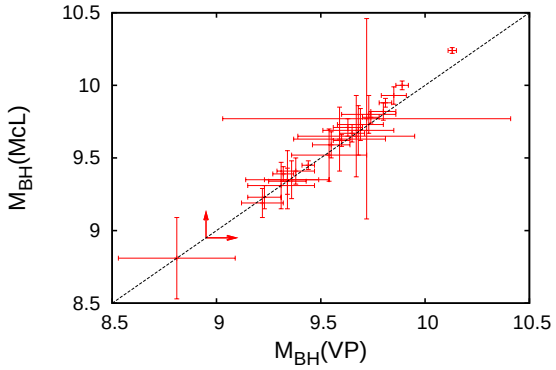

Fig. 4. Comparison of $M_{\rm BH}$ derived from a different formula (Table 6). The abscissa and ordinate are the values derived based on Vestergaard & Peterson (2006), and McLure & Jarvis (2002), respectively. Arrows mean lower limits. The dashed line represents a 1:1 correspondence.

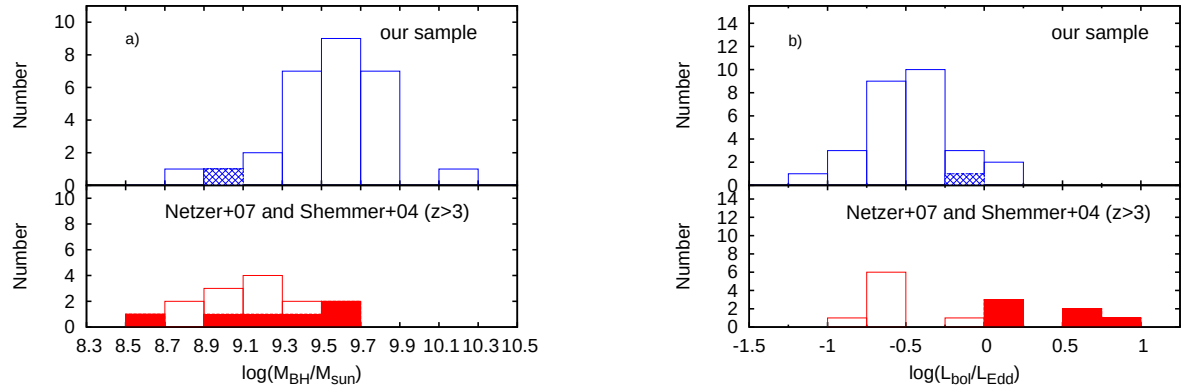

Fig. 5. (a) Histogram of $M_{\rm BH}$ estimated in this study (upper panel) and in the literature (Netzer et al. 2007; Shemmer et al. 2004) for only $3 < z < 4$ sources (lower panel). A lower limit object is shown as a shaded area. (b) Comparison of the $L_{\rm bol}/L_{\rm Edd}$ distribution for our sample (upper panel) and Netzer's sample at $z > 3$ (lower panel). An upper limit object is displayed by a shaded area. In the lower panels of both a) and b), open and filled histograms correspond to Netzer's sample and Shemmer's sample, respectively.

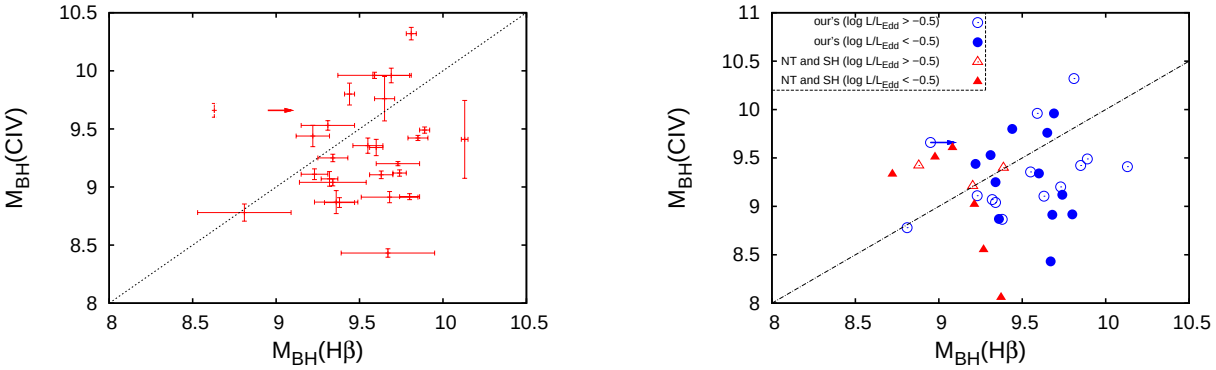

Fig. 6. Left: Comparison of the SMBH masses ($M_{\rm BH}$) estimated from the Hβ method (abscissa) and the C IV method (ordinate). C IV data are from Shen et al. (2011). Two QSOs are not plotted here due to lack of C IV data. The right arrow means a lower limit. The dashed line represents a 1:1 correspondence. Right: The same plot as the left figure but with the Eddington ratio information added. The open blue circles are targets with high Eddington ratios with $\log(L_{\rm bol}/L_{\rm Edd}) > -0.5$. The filled blue circles are those with low Eddington ratios with $\log(L_{\rm bol}/L_{\rm Edd}) < -0.5$. The open red triangles correspond to Netzer and Shemmer's sample which has a high Eddington ratio of $\log(L_{\rm bol}/L_{\rm Edd}) > -0.5$. The filled red triangles are those with low Eddington ratios of $\log(L_{\rm bol}/L_{\rm Edd}) < -0.5$. For two QSOs in our sample and five QSOs in Netzer and Shemmer's sample, C IV data are not available in Shen et al. (2011). The right arrow indicates a lower limit. We find that samples with high Eddington ratios appear to be distributed in the upper-left side compared to those with low Eddington ratios which distribute in both the upper-left and lower-right sides.

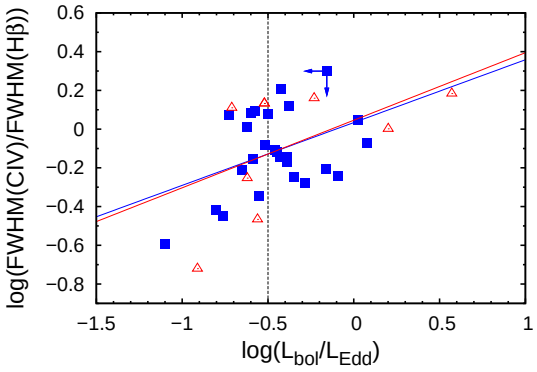

Fig. 7. Relationship between Eddington ratio (abscissa) and the FWHM(C IV) to FWHM(Hβ) ratio (ordinate) . The filled blue boxes show our sample, and the open red triangles show the sample of Netzer et al. (2007) and Shemmer et al. (2004). Two QSOs in our sample and five QSOs in Netzer and Shemmer's sample are not plotted here because C IV data are not available in Shen et al. (2011). The blue line represents the best fit for our sample only. The red line shows the best fit for combined samples (ours, Netzer's, and Shemmer's). Arrows mean upper limits. The dashed line represents the border between the high and low Eddington ratios.